Bonding in the molybdenum silicides

A. K. McMahan and J. E. Klepeis
Lawrence Livermore National Laboratory, University of California, Livermore, California 94550

M. van Schilfgaarde
SRI International, 333 Ravenswood Avenue, Menlo Park, California 94025

M. Methfessel
Institut für Halbleiterphysik, P. O. Box 409, D-15204 Frankfurt an der Oder, Germany
(Received 14 December 1993; revised manuscript received 23 June 1994)

Full-potential linear muffin-tin orbital calculations are reported for the bulk properties, density of states, and electron density in $A2$ Mo, $A15$ Mo_3Si, $D8_m$ Mo_5Si_3, $C11_b$ $MoSi_2$, and $A4$ Si. Both the magnitude and the directional anisotropy of the valence charge density associated with bonds in the three silicides suggest a hierarchy in bond strength, ordered from strongest to weakest: Mo-Mo, Mo-Si, and Si-Si. A combined Mulliken and tight-binding analysis shows this behavior to coincide with variations in occupation of the respective types of bonding states, which is ultimately traced to Mo($4d$) site energies that are nearly degenerate with the Fermi level, in contrast to Si($3p$) site energies lying about 5 eV higher. These characteristics point to the dominance of Mo-Si bonding in $C11_b$ $MoSi_2$, consistent with the near pd hybridization gap in this material, which appears to explain the unique position of the disilicide in systematics of the molybdenum silicide bulk properties. Finally, having identified the critical elements of the electronic structure in the molybdenum silicides, this work provides a physically motivated basis upon which to improve models used in the study of large-scale Mo-Si interface problems.

I. INTRODUCTION

The Mo-Si system has diverse technological application to high-reflectance x-ray optical elements,[1-6] gates and interconnections in very large-scale integrated circuits[7-13] and high-temperature structural materials.[14-19] These applications are favored in general by different physical properties. The modulation of electron density in the direction of appropriately chosen bilayer periodicity has been shown to lead to high reflectance of Mo-Si multilayers in the soft x-ray region of 13–20 nm,[1,2] prompting growth and characterization studies of these systems.[3-6] The low resistivity, high melting temperature, and processing compatibility with silicon technology makes $MoSi_2$ one of a number of promising materials for use as interconnections in Si device applications,[7-8] stimulating detailed studies of $MoSi_2$ films on Si surfaces.[9-13] The low density and high melting temperature of molybdenum disilicide, combined with its high-temperature strength and oxidation resistance, have also aroused strong interest in $MoSi_2$ or $MoSi_2$ composites as advanced structural materials for service in the range 1200–1600 °C.[14-19]

An issue common to many of these applications is the nature of the interface between Mo and Si, or between these elements and the molybdenum silicides. Although atomically abrupt Mo-Si interfaces are desired in the x-ray mirror applications, intervening layers often of stoichiometry $MoSi_2$ are formed,[4-6] while Mo_5Si_3 interlayers can occur for high annealing temperatures[5,9,13] and at $MoSi_2$-metal interfaces.[17] The characteristics of such interfacial layers — stoichiometry, thickness, whether amorphous or crystalline — are highly process dependent.

The ability to model and evaluate the different processing strategies would be highly beneficial. Molecular dynamics simulations of the deposition of Mo on Si and vice versa have already been performed using analytic atom-atom potentials including three-body terms.[20] This work correctly reproduced the observed asymmetry between Mo-on-Si and Si-on-Mo interlayer thicknesses, but refrained from detailed quantitative comparisons with experiment due to the crudeness of the interatomic potential models. It is the ultimate goal of our effort to provide a more realistic tight-binding representation of the interatomic forces in the binary Mo-Si system for use in such simulations.[21] First, however, we report in this paper a thorough examination of the nature of bonding in this system, paying particular attention to the implications of these results for physically realistic values of the more important tight-binding parameters.

The present paper reports *ab initio* local density functional calculations of the bulk properties, one-electron density of states (DOS), and electron charge density for $A2$ (bcc) Mo, $A15$ Mo_3Si, $D8_m$ Mo_5Si_3, $C11_b$ $MoSi_2$, and $A4$ (cubic diamond) Si. These include all bulk-stable phases in the Mo-Si system, except for a high-temperature $MoSi_2$ phase (space group $C6_22$) which is stable above 1900 °C.[22] We do not consider the metastable, hexagonal $C40$ stacking variant

of tetragonal $C11_b$ $MoSi_2$ which is a common structure for thin $MoSi_2$ films subjected to low annealing temperatures.[9-13] There have been numerous previous calculations of the bulk properties and/or electronic structure for individual group-V (Refs. 23 and 24) and group-VIII (Refs. 25–29) transition metal silicides, and stoichiometry surveys for various $3d$ and $4d$ silicides based on simple high symmetry structures.[30-32] Previous calculations for the molybdenum silicides have been carried out for both the $C11_b$ phase[33-38] and the metastable $C40$ phase[37-39] of $MoSi_2$. The superconducting behavior of A15 Nb_3Ge also motivated earlier surveys of A15-structure transition metal germanides, silicides, and related materials,[40-43] including Mo_3Si.[40]

Generic characteristics of the electronic structure of the transition metal silicides include low-lying Si($3s$) states and strong transition metal d-Si($3p$) hybridization within 5 eV or so of the Fermi level.[23-43] In contrast to the stoichiometry surveys carried out for simple high symmetry structures,[30-32] our calculations for the observed molybdenum silicide phases show more pronounced effects of such pd hybridization. While also evident in the Mo-rich silicides, the most dramatic manifestation is the very low DOS at the Fermi level in $C11_b$ $MoSi_2$, which we argue to be nearly a pd hybridization gap. Since the miscibility of Mo and Si depends on sufficient strength and prevalence of Mo-Si bonds, one might expect prominent evidence of Mo-Si interactions in the observed stable silicide structures. Certainly Mo-Si bonds are prevalent in the three molybdenum silicides, since an average atom in these materials has 6–7 unlike neighbors within 5.3 bohr (2.8 Å).

By using an implementation[44,45] of local density functional theory which makes no shape approximation to the one-electron potential, we are able to provide a quantitative comparison of the valence charge density in all reasonably short bonds across the five member series. We find for the silicides a systematic hierarchy, Mo-Mo, Mo-Si, and Si-Si, in order of greatest to least charge density in bonds of the same length. Directional anisotropy of the charge density in the vicinity of Si atoms also favors Mo over Si neighbors in a disproportionate manner, which is consistent with this hierarchy. These features are not simply due to overall differences in $|\phi|^2$ of the respective Mo($4d$) and Si($3p$) orbitals since a superposition of free atom electron densities yields differences between the various bond types which are dramatically (a factor of three or more) reduced. Given that superposed free atom electron densities are limited to the form $|\phi_a|^2+|\phi_b|^2$ (to use a two-site, two-electron analogy), one obvious potential contributor to these features would be bonding cross terms, $2\,\mathrm{Re}\,[\phi_a^*\phi_b]$, in the self-consistent charge density of the form $2\,|(\phi_a+\phi_b)/\sqrt{2}|^2$, in which case the variations in bond charge density would truly reflect relative bond strengths.

The distribution in energy of the bonding cross terms may be examined by a Mulliken population analysis,[46] which for convenience we carry out in modified form using a reduced, orthogonalized basis. The results show significant bond-antibond separation for all Mo($4d$)-Mo($4d$), Mo($4d$)-Si($3p$), and Si($3p$)-Si($3p$) overlaps that we have examined, with the Mo-Mo bonding and antibonding state densities lying roughly equidistant from the Fermi level, below and above, respectively. Simple interrelationships (described in the Appendix) between the various Mulliken functions and tight-binding parameters show that the Mo($4d$) site energies, ε_d, are indeed close to the Fermi level, ε_F, whereas the Si($3p$) site energies, ε_p, are about 5 eV higher. Since the bond/antibond crossover for dd, pd, and pp couplings will occur in first approximation at $\varepsilon_d < \frac{1}{2}(\varepsilon_p+\varepsilon_d) < \varepsilon_p$, respectively, and $\varepsilon_F \sim \varepsilon_d$, these relative site-energy positions suggest that decreasing fractions of the available bonding states will be occupied in the three cases. This perspective is complicated by differences in the size of the corresponding intersite electronic couplings (hopping parameters); however, we argue in this paper that the site energy difference $\varepsilon_p-\varepsilon_d \sim 5$ eV is the most likely underlying cause of the bond hierarchy documented in the electron density. It might also be noted that the intersite couplings are sufficiently large so that the molybdenum silicides are still primarily covalent rather than ionic, in spite of the site energy difference.

One implication of the bond hierarchy discussed here is that $C11_b$ $MoSi_2$, which has no short Mo-Mo distances and twice as many Mo-Si as Si-Si bonds, is a manifestation of predominant Mo-Si bonding. This view suggests an interpretation of the bulk properties of the molybdenum silicides. The equilibrium volumes, V_0, when plotted per atom, show a gradual and smooth decrease from Mo to $MoSi_2$, followed by a rather abrupt increase to Si. We interpret this behavior as an interpolation between dominant Mo-Mo to dominant Mo-Si bonding throughout the sequence Mo-Mo_3Si-Mo_5Si_3-$MoSi_2$, followed by Si-Si bonding in pure Si. Similarly, since the tendency of Mo and Si to form compounds depends on the comparative strength and prevalence of the unlike Mo-Si interactions, this perspective is also consistent with the disilicide having the most negative heat of formation, H_f, of any of the molybdenum silicides.

In the remainder of this paper, Sec. II reviews the crystal structures of the molybdenum silicides; and Sec. III, our local-density functional computational methods. Calculated values for the bulk properties of the molybdenum silicide series are presented in Sec. IV; the total and partial densities of states, in Sec. V. Results of our examination of the charge density across the five member series, in regard both to midbond values and directional anisotropy, are presented in Sec. VI. A combined Mulliken population analysis and tight-binding interpretation of these results is given in Sec. VII, making use of interrelationships between various Mulliken functions and tight-binding parameters as described in the Appendix. Finally, our summary comments and conclusions are given in Sec. VIII.

II. CRYSTAL STRUCTURES

The crystal structures of the three molybdenum silicides are indicated in Table I, along with the pure Mo and Si end members.[22] Throughout this paper we use the

TABLE I. Structural characterization of the molybdenum silicides and end members. The space group (name and number), site (multiplicity and Wyckoff letter), and the first site position follow Ref. 48. Muffin-tin radii, R, are given in units of the Wigner-Seitz radius, R_{WS}. Experimental values used for the internal parameters of the two tetragonal structures are given in parentheses after these structures.

Material	Structure	Space group		Site		1st position	R/R_{WS}
Mo	$A2$	$Im\bar{3}m$	229	Mo	$2a$	$0,0,0$	0.879
Mo_3Si	$A15$	$Pm\bar{3}n$	223	Mo	$6c$	$\frac{1}{4},0,\frac{1}{2}$	0.806
				Si	$2a$	$0,0,0$	0.996
Mo_5Si_3	$D8_m$	$I4/mcm$	140	Mo	$4b$	$0,\frac{1}{2},\frac{1}{4}$	0.816
				Mo	$16k$	$x,y,0$	0.911
				Si	$4a$	$0,0,\frac{1}{4}$	0.816
				Si	$8h$	$x,x+\frac{1}{2},0$	0.784
	($c/a=0.50916$, $x_k=0.075$, $y_k=0.224$, $x_h=0.165$)[a]						
$MoSi_2$	$C11_b$	$I4/mmm$	139	Mo	$2a$	$0,0,0$	0.887
				Si	$4e$	$0,0,z$	0.886
		($c/a=2.4519$, $z=0.333$)[a]					
Si	$A4$	$Fd\bar{3}m$	227	Si	$8a$	$\frac{1}{8},\frac{1}{8},\frac{1}{8}$	0.698

[a]Reference 49, p. 2771.

Strukturbericht labels[47] $A2$ (bcc), $A15$, $D8_m$, $C11_b$, and $A4$ (cubic diamond) for these Mo, Mo_3Si, Mo_5Si_3, $MoSi_2$, and Si phases, respectively. Each structure is characterized by a particular space group and one or more sets of symmetry-equivalent atom positions, as indicated by the numbers of atoms and Wyckoff letters in the "site" column. The former multiplicities are for conventional unit cells, and should be divided by 1, 2, and 4 to obtain the corresponding primitive cell values for P (primitive), I (body centered), and F (face centered) space groups, respectively. The first atom position in each Wyckoff set is given in Table I; complete lists are found elsewhere.[48,49] Since the present structures are all cubic ($A2$, $A15$, and $A4$) or tetragonal ($D8_m$ and $C11_b$), the positional notation "x,y,z" designates Cartesian coordinates xa, ya, and zc, where a and c ($c=a$ for cubic) are lattice constants. We have taken experimental values for all internal parameters, that is, c/a, x_k, y_k, and x_h for $D8_m$, and c/a and z for $C11_b$.[49] Muffin-tin radii, R, are given for each inequivalent site, relative to the Wigner-Seitz radius, R_{WS}, where the volume per atom (averaged over all atoms) is $4\pi R_{WS}^3/3$. These radii lead to packing fractions of 0.64, 0.63, and 0.70 for the $A15$, $D8_m$, and $C11_b$ cases, respectively, which may be compared to 0.68 for $A2$ (bcc) and 0.34 for A4 (cubic diamond). The molybdenum silicides are thus seen to be relatively close packed.

Two c-axis cross sections are shown for each of the three silicide structures in Fig. 1(a)–1(f), where circles and squares indicate Mo and Si atoms, respectively. These two types of layers alternate as they are stacked in the c direction, except that for the $A15$ and $D8_m$ cases, the large square in Fig. 1(a) and the dotted rectangles in Fig. 1(c) are rotated in the plane of the paper by 90° about their individual centers for layers at $z=\pm\frac{1}{2}c$, $\pm\frac{3}{2}c$, and so on. The $D8_m$ structure has four inequiva-

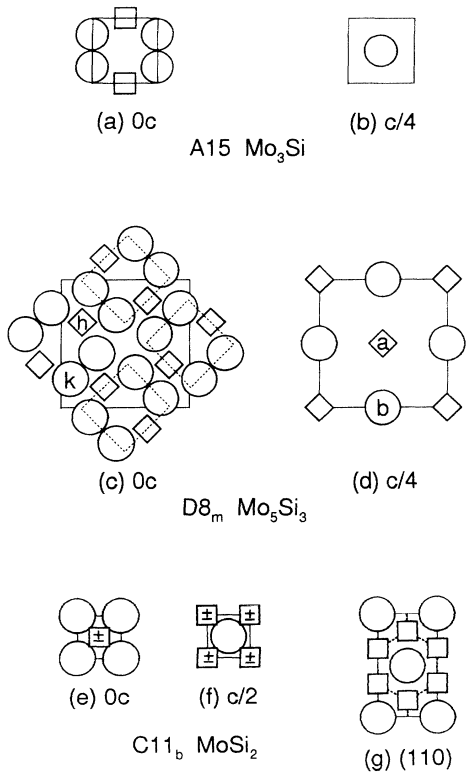

FIG. 1. C-axis cross sections for the three molybdenum silicides: (a), (b) $A15$ Mo_3Si, (c), (d) $D8_m$ Mo_5Si_3, and (e), (f) $C11_b$ $MoSi_2$. A (110) cross section of the $C11_b$ phase is shown in (g). Mo (Si) atoms are indicated by circles (squares or diamonds), and ± indicate atoms above or below the cross sectional plane.

lent sites, labeled by the Wyckoff letters as shown. Atoms outside of the $D8_m$ unit cell (solid square) are shown in Fig. 1(c), and the $A15$ unit cell boundaries are shifted in Figs. 1(a) and 1(b) relative to their Table I placement, in order to emphasize similarities between these two structures.[50] In particular, it is clear that the $D8_m$ Mo-b site has essentially the same local environment as Mo in the $A15$ structure. Both types of Mo atoms ($A15$ and $D8_m$ b), as well as the $D8_m$ Si-a atoms, form chains exhibiting the smallest interatomic separations in their respective structures, as seen in Figs. 2(a) and (b), respectively. These chains point along all three Cartesian directions in cubic $A15$, but only along the **c** direction in tetragonal $D8_m$. The $\pm$ inserts for the $C11_b$ Si sites in Figs. 1(e) and 1(f) indicate atoms above and below the planes shown. A (110) cross section in Fig. 1(g) suggests graphiticlike layers of Si atoms in this perspective of the $C11_b$ structure, with a Mo atom in the center of each hexagon. Note, however, that each Mo and Si atom has approximately ten near neighbors in the $C11_b$ structure, as seen in Figs. 2(c) and 2(d), respectively.

For the purposes of later discussion, we note that each Mo site in the $A15$ phase has two Mo first, four Si second, and eight Mo third neighbors ($d^{(1)} = 4.57$, $d^{(2)} = 5.11$, $d^{(3)} = 5.60$ bohr), as shown in Fig. 2(a). The $D8_m$ Mo b site has relatively closer Si second neighbors ($d^{(1)} = 4.60$, $d^{(2)} = 4.80$, $d^{(3)} = 5.65$ bohr). Each Si a site in the $D8_m$ phase has two Si first and eight Mo second neighbors ($d^{(1)} = 4.60$, $d^{(2)} = 4.84$ bohr), as shown in Fig. 2(b). Each Si atom in the $C11_b$ disilicide has five Mo and five Si near neighbors as shown in Fig. 2(d). There are four inequivalent types of bonds (Si-Mo versus Si-Si and lateral versus **z** direction); however, the corresponding distances differ by 0.4% or less for the parameters in Table I, so that the central Si in Fig. 2(d) and the Mo in Fig. 2(c) each has effectively ten near neighbors ($d = 4.9$ bohr). All interatomic distances cited here and throughout this paper were obtained using the internal parameters in Table I, combined with the theoretical equilibrium volumes to be given shortly, and are in atomic units (1 bohr = 0.529 177 Å). It is worth noting that there are only three types of relatively short Si-Si bonds in the molybdenum silicides, that in Fig. 2(b), and the two (lateral and **z** direction) in Fig. 2(d).

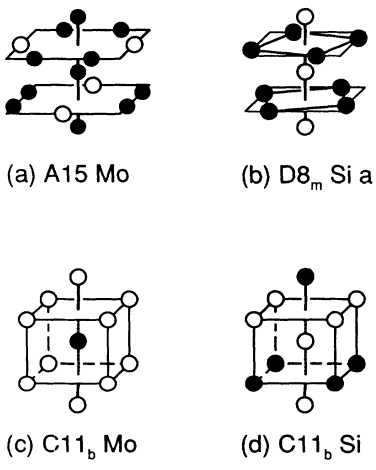

FIG. 2. Local environments of two Mo and two Si sites in the molybdenum silicides. Mo (Si) atoms are shown by filled (open) circles.

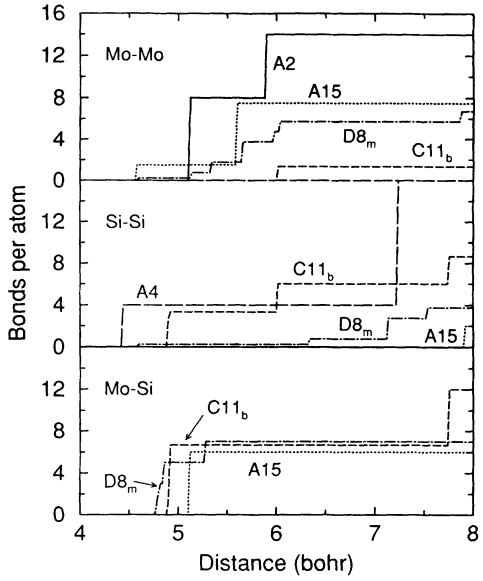

FIG. 3. Coordination of an average atom in the five member Mo-Si series, as a function of distance, and subdivided into bond type.

The relative proportions of Mo-Mo, Si-Si, and Mo-Si bonds, as we shall loosely refer to atom pairs at a given distance, may be deduced from Fig. 3, where

$$n(d) \equiv \frac{2}{N} \sum_{i<j} \theta(d - |\mathbf{R}_i - \mathbf{R}_j|) \tag{1}$$

is resolved into the three separate contributions. Here i ranges over all (Mo and Si) N atoms at positions $\mathbf{R}_i$. The quantity $n(d)$ is the coordination number as a function of distance, d, for the $A2$ Mo and $A4$ Si end members, but represents an *average* atom for the silicides. There are 8–10 neighbors per such average atom in the silicides for d somewhat larger than the $A2$ Mo near-neighbor distance (e.g., $d = 5.3$ bohr, ~4% larger), consistent with the large packing fractions noted above. Based purely on bond length and prevalence, one might judge from Fig. 3 that the dominant bonding components in the five structures would be $A2$ (Mo-Mo), $A15$ (Mo-Mo, Mo-Si), $D8_m$ (Mo-Si, Mo-Mo), $C11_b$ (Mo-Si, Si-Si), and $A4$ (Si-Si).

III. CALCULATIONAL METHODS

The calculations presented in this paper were carried out using a full-potential linear muffin-tin orbital (FP-LMTO) implementation of the local-density approximation (LDA). The method has been described in detail elsewhere.[44,45] It makes no shape approximation to the

one-electron potential; however, for computational convenience, it divides space into volumes within nonoverlapping muffin tin spheres plus the encompassing interstitial region. The basis functions are atom-centered augmented (spherical) Hankel functions, which are numerical solutions of the Schrödinger equation inside each muffin tin that are matched (slope and value) onto Hankel function tails extending into the adjoining interstitial region. The augmented Hankel functions are characterized by their atom center (basis site $\mathbf{q}$), by their principle, angular, and magnetic quantum numbers (n, l, and m, respectively), and by the decay constant, κ, of the exponential factor, $e^{-\kappa r}$, in the Hankel function tails. Accurate treatment of the interstitial region is insured in this method by the use of expanded "multiple-κ" basis sets in which up to three augmented Hankel functions, of differing decay constants, are used to represent each atomic orbital characterized by $\mathbf{q}$, n, l, and m. The accuracy of this approach for both bulk properties and electron charge densities has been demonstrated elsewhere.[45]

A. Bulk properties, total DOS, and charge density

All results presented in this paper for the bulk properties (equilibrium volume, V_0, cohesive energy, $E_{\rm coh}$, and bulk modulus, B_0), for the total DOS, $D(\varepsilon)$, and for the valence charge density, $\rho(\mathbf{r})$, were obtained from highly accurate multiple-κ FP-LMTO calculations as will now be described.

The molybdenum silicide valence states are of predominant Mo($4d$) and Si($3sp$) character. In the present calculations, we have used 29 augmented Hankel functions per Mo site [s (3 κ's), p (3 κ's), d (2 κ's), and f (1 κ)]; and 22, per Si site [s (3 κ's), p (3 κ's), and d (2 κ's)], where the corresponding decay energies are $-\kappa^2 = -0.01$ ($spdf$), -1.0 (spd), and -2.3 Ry (sp). Table II indicates the convergence with basis size of our valence charge densities, $\rho(\mathbf{r})$, along the z-direction near-neighbor Mo-Si and Si-Si bonds in $C11_b$ $MoSi_2$. Here the largest difference, $\Delta\rho$, is reported between values of $\rho(\mathbf{r})$ obtained by the indicated basis in comparison to our standard choice just mentioned (also the first line of table), considering all points $\mathbf{r}$ along the bond axis and more than 0.7 bohr away from each atom. The largest difference found throughout this range for the triple-κ and each of the double-κ bases occurs near the midbond point, and the corresponding $\Delta\rho$ values are given in the table. The largest difference encountered throughout this range for each of the single-κ bases, however, occurs near one of the outer valence maxima (to be defined in Sec. VI). For completeness, we have therefore given values of the difference function $\Delta\rho(\mathbf{r})$ at all extrema found throughout the indicated range for each of the single-κ cases. For the Mo-Si bond, these extrema occur near the Mo outer valence maximum, near the Mo-Si midbond, and near the Si outer valence maximum, respectively, and similarly for the Si-Si case. These results suggest that even double-κ charge densities are reasonably accurate with the precise values of the decay energies not overly crucial. They suggest that the charge densities calculated in this paper (which use three κ's to represent each s and p atomic orbital) are converged to better than 0.3 millielectrons/bohr^3.

Accurate calculation of the bulk properties for these materials also requires extended treatment of the Mo($4p$) states. We have therefore included a second "semicore" panel to provide bandlike representation of both the Mo $4s$ and $4p$ states, using the same Mo and Si bases as for the upper panel, except for the appropriate reduction in the Mo s and p principle quantum numbers, and the omission of Mo f states in this lower panel. We found the equilibrium volume of $A2$ (bcc) Mo to be reduced by 0.5% when Mo f functions were added to the basis for the upper panel, and by 1.0% when Mo d functions were added to the basis for the semicore panel, and have therefore retained these functions in the respective bases. Linearization energies were taken to be centers of gravity

TABLE II. Charge density convergence tests for the present multiple-κ FP-LMTO calculations, as carried out along the z-direction Mo-Si and Si-Si bonds in $C11_b$ $MoSi_2$. The quantities $\Delta\rho$ (in millielectrons/bohr^3) show the largest differences in valence charge density found along the bond axis in between these atoms, and more than 0.7 bohr away from each atom, as obtained for the listed basis relative to our standard choice (first line of table). Three extrema in the difference function $\Delta\rho(\mathbf{r})$ are given for the two single-κ cases, as discussed in the text. The numbers 1 (first), 2 (first two), and 3 (all three) under the s, p, d, and f headings specify those $-\kappa^2$ values (in Ry) characterizing the augmented Hankel functions used to represent an atomic orbital of the indicated angular momentum, both for Mo and Si (same without f states) sites.

$-\kappa^2$	s p d f	$\Delta\rho$(Mo-Si)	$\Delta\rho$(Si-Si)
-0.01, -1, -2.3	3 3 2 1	0	0
-0.50, -1, -2.3	3 3 2 1	0.2	0.1
-0.01, -1	2 2 2 1	0.3	0.1
-0.50, -1	2 2 2 1	0.9	0.3
-0.01	1 1 1 1	19.2	5.1
		-1.8	-2.2
		6.4	5.1
-0.50	1 1 1 1	31.1	11.3
		-2.0	-3.9
		13.0	11.3

of the appropriate occupied partial state densities,[51,52] except for the Mo $5p$ case, where an energy corresponding to a logarithmic derivative of ~ 0.7 was used. The Brillouin zones were sampled with 72 (8), 84 (10), 59 (6), 163 (13), and 60 points per irreducible wedge for the upper (semicore) panels of the $A2$, $A15$, $D8_m$, $C11_b$, and $A4$ phases, respectively. Comparisons with results obtained from smaller samplings suggest that these choices give total energies accurate to 0.01 eV/atom or better. All lower-lying states were treated self-consistently in an atomiclike mode.

The present FP-LMTO method makes use of a separate expansion of the electron *density* associated with each panel, in terms of atom-centered, and possibly also interstitial-sphere-centered, augmented Hankel functions.[44,45] We have used 98 functions per site in these expansions, corresponding to two decay energies, $-\kappa^2 = -1$ and -3 Ry, and $l_{\max} = 6$. A smaller $l_{\max} = 4$ value of this cutoff reduces the cohesive energy of $MoSi_2$ by only 1%, and increases its equilibrium volume by only 0.4%, so that the larger value taken here should be more than adequate. The metals (Mo and the three silicides) are all relatively close packed, and so interstitial or empty spheres were not required for these expansions. For $A4$ (cd) Si, however, augmented Hankel functions centered in empty spheres placed at the usual tetrahedral interstitial sites were used in the expansion of the charge density. The muffin-tin radii used in this work were generally taken to be 1–2 % smaller than the values given in Table I, which correspond to touching muffin tins.

All LDA results reported in this work are from scalar relativistic calculations which used the exchange-correlation potential of Hedin and Lundqvist.[53] Total energy calculations were carried out for each of the five materials at seven volumes, corresponding to the experimental equilibrium volume and that increased/decreased by 2%, 4%, and 6%. These results were fit by a four-term Birch-Murnaghan equation of state[54] in order to obtain the theoretical equilibrium volume, V_0, cohesive energy, $E_{\rm coh}$, and bulk modulus, B_0. Additional self-consistent calculations were performed at the theoretical V_0 to provide the DOS and valence charge density results shown in this paper. In order to emphasize bonding characteristics, "valence" charge density results presented here *exclude* the core and semicore contributions unless specifically indicated otherwise.

Total energies for the isolated Mo and Si atoms required for the $E_{\rm coh}$ calculations were obtained from appropriate spin-polarized treatments.[53] In particular, our results for the isolated atom total energies are $E_{\rm Mo}(5s^1 4d^5) = -8088.921\,31$ Ry and $E_{\rm Si}(3s^2 3p^2) = -577.696\,58$ Ry. We have also tested the gradient correction of Langreth, Mehl, and Hu,[55] for the bulk properties only, and in this case our corresponding spin-polarized isolated atom energies are $E_{\rm Mo}(5s^1 4d^5) = -8092.204\,12$ Ry and $E_{\rm Si}(3s^2 3p^2) = -578.533\,55$ Ry.

B. Mulliken decomposition of the DOS

Mulliken decomposition[46] of the total DOS, $D(\varepsilon)$, is an inherently basis-dependent procedure which nevertheless has considerable interpretive value, especially when carried out using relatively small bases. For this reason, and to facilitate the tight-binding analysis of Sec. VII, we have performed all Mulliken decompositions using reduced bases with only *one* augmented Hankel function per $\mathbf{q}nlm$ atomic orbital ("single-κ" calculation), with a -0.5 Ry decay energy to provide a sufficient degree of localization. The accurate multiple-κ self-consistent potential was still used in both generating these augmented Hankel functions and assembling the one-electron Hamiltonian and overlap matrices. The Mulliken partial DOS's were then constructed from solutions of these eigenvalue problems.

Such reduced-basis Mulliken decompositions are legitimate only insofar as the single-κ total DOS's agree reasonably closely with the fully accurate multiple-κ $D(\varepsilon)$, which we emphasize is indeed the case here for the relatively *close-packed* phases, i.e., Mo and all three silicides. For these phases the single-κ and accurate multiple-κ total DOS's have essentially identical features although offset in energy at some places by up to 0.2 eV. Compared to valence band widths (bottom up to the Fermi level) over 10 eV, this is quite respectable, and compares favorably to typical tight-binding band structure fits, which would be an alternate approach to the present analysis. The rather good single-κ agreement with the fully accurate total DOS is also consistent with the general success of LMTO atomic-sphere approximation[51,52] calculations for the bulk properties and DOS's of close-packed solids, including $MoSi_2$.[35,37] The single-κ basis is less satisfactory for *open-packed* $A4$ (cd) Si, yielding a too-large (3 eV) semiconducting gap. This deficiency, however, does not compromise our interpretive analysis for the three silicides, the materials which are the primary focus of the present paper.

We have performed two kinds of Mulliken decompositions in this paper. First, we resolve the total DOS's into separate Mo and Si components (Sec. V) using the standard (nonorthogonal basis) expression for Mulliken site-lm decomposition of the DOS,[46] as has been described in previous FP-LMTO applications.[56] We ameliorated the effect of our reduced atom-centered basis on this $A4$ Si decomposition by adding basis functions (one per lm) also in the interstitial spheres. Second, for the silicides, we have also performed decompositions into partial DOS's which are analogous to Mulliken overlap populations[46] (Sec. VII). As discussed in the Appendix, we transform to an orthogonal basis for this decomposition in order to exploit simple relationships that exist between these appropriately modified Mulliken partial DOS's and tight-binding parameters. The orthogonal basis is defined by

$$H_{\rm or} = O^{-1/2} H O^{-1/2} , \tag{2}$$

where H and O are the Hamiltonian and overlap matrices, respectively, corresponding to the reduced, nonorthogonal augmented Hankel functions basis. While other first-principles tight-binding methods might be more accurate,[57] the basis defined by Eq. (2) provides an extremely convenient framework within which to as-

sess overall characteristics of the molybdenum silicides in terms of simple tight-binding concepts.

IV. BULK PROPERTIES

We present here our calculated LDA results for the $T = 0$, equilibrium (zero pressure) volume V_0, cohesive energy $E_{\rm coh}$, bulk modulus B_0, and heat of formation ΔH_f, for the five member Mo/Si series. Our values for the first three quantities are summarized in Table III, while plots of ΔH_f and V_0 are given in Figs. 4 and 5, respectively. All $E_{\rm coh}$, B_0, and ΔH_f values in the table and in these figures correspond to theoretical V_0's. Since there is not sufficient information to make lattice dynamical corrections for all members of the present series, our theoretical results are $T=0$ values, uncorrected for zero-point motion, whereas experimental values are for room temperature, except as will be noted for $E_{\rm coh}$. There is no evidence, however, that the 298-K lattice dynamical corrections are large.[61,62] After discussing previous LDA calculations for the disilicide, comparison between theory and experiment is made for the whole series. We consider both standard LDA and one particular gradient correction which is currently available in our FP-LMTO code, namely, that of Langreth, Mehl, and Hu (LMH),[55] which, on the whole, improves agreement with the data. Note that all extensive quantities (V_0, $E_{\rm coh}$, and ΔH_f) are reported *per atom* in the present paper, i.e., divided by the total number of atoms irrespective of their Mo or Si identity.

Previous LDA calculations of the bulk properties of the stable molybdenum silicides have been carried out only for the $C11_b$ disilicide.[33–38] The spread (including our result) in these values for the disilicide $E_{\rm coh}$ is 0.2 eV/atom (3%),[33–38] with our value the largest, although essentially identical to that of Bhattacharyya and co-workers.[33] The spread for V_0 is 3.7 bohr^3/atom (4%),

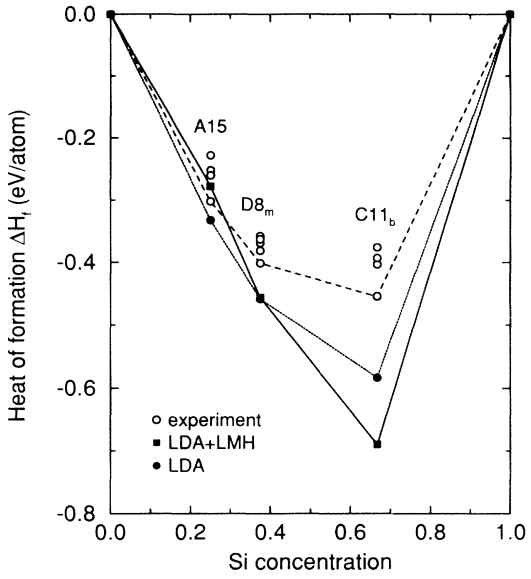

FIG. 4. Measured (open circles) and calculated (filled symbols) heats of formation for the molybdenum silicides. Experimental data are from Refs. 63–66, while "LMH" designates use of the Langreth-Mehl-Hu gradient correction, Ref. 55.

TABLE III. Cohesive energy, $E_{\rm coh}$, equilibrium volume, V_0, and bulk modulus, B_0, for the molybdenum silicide series. Calculated $T = 0$ values are labeled by "LDA" and "LDA+LMH", where the latter indicates use of the Langreth-Mehl-Hu gradient correction. Experimental values for $E_{\rm coh}$ are for $T=0$; V_0 and B_0, room temperature.

$E_{\rm coh}$ (eV/atom)		LDA	LDA+LMH	Expt.
$A2$	Mo	7.63	6.22	6.82[a]
$A15$	Mo_3Si	7.35	6.10	6.52[b]
$D8_m$	Mo_5Si_3	7.17	6.08	6.37[b]
$C11_b$	$MoSi_2$	6.58	5.85	5.78[b]
$A4$	Si	5.18	4.63	4.63[a]
V_0 (bohr^3/atom)				
$A2$	Mo	102.4	103.8	105.2[c]
$A15$	Mo_3Si	95.4	97.2	98.6[c]
$D8_m$	Mo_5Si_3	93.6	95.1	96.3[c]
$C11_b$	$MoSi_2$	88.3	89.5	90.5[c]
$A4$	Si	133.3	135.9	134.9[c]
B_0 (GPa)				
$A2$	Mo	289.8	281.3	260.8[d]
$A15$	Mo_3Si	253.4	245.6	
$D8_m$	Mo_5Si_3	260.8	251.1	
$C11_b$	$MoSi_2$	223.4	223.5	209.7[e]
$A4$	Si	95.2	93.1	98.8[a]

[a]Reference 58.
[b]See text.
[c]Reference 49, pp. 2748, 2771, and 3188.
[d]Reference 59.
[e]Reference 60.

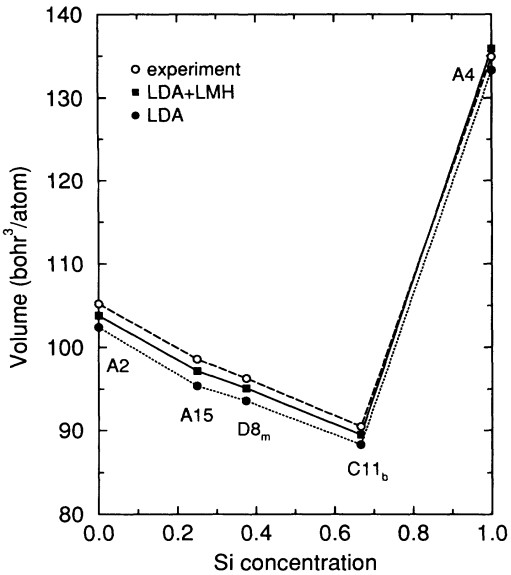

FIG. 5. Measured (open circles) and calculated (filled symbols) equilibrium volumes for the five member Mo-Si series. Experimental data are from Ref. 49, while "LMH" designates use of the Langreth-Mehl-Hu gradient correction, Ref. 55.

with our value the smallest, 1 bohr^3/atom smaller than found by Alouani and co-workers.[36] We believe that self-consistent treatment of the Mo($4p$) semicore levels is important, and note that the two largest reported values of the disilicide V_0, 92.0 and 90.5 bohr^3/atom, were obtained using frozen core states[38] and core states replaced by a pseudopotential,[33] respectively. The primary difference between our results and those of Alouani *et al.*,[36] who use the same FP-LMTO method, is our scalar relativistic versus their nonrelativistic treatment. We also use a larger basis (d states in the semicore and f states in the valence bands) and more interstitial fitting functions ($l_{\max} = 6$ rather than $l_{\max} = 4$). All of these differences enhance binding, i.e., larger $E_{\rm coh}$ and smaller V_0. In regard to B_0, note that Alouani *et al.*[36] also calculated values for all six independent elastic constants, which were found to be in excellent agreement with experiment.[60] Both Alouani *et al.*[36] and Mattheiss[38] carried out some optimization of the two internal parameters, c/a and z, for $C11_b$ $MoSi_2$, finding values within 0.2% and 0.8%, respectively, of the choices assumed in this work. Calculated values reported[34,36,38] for the $MoSi_2$ heat of formation are in the range $-\Delta H_f = 0.48$–0.62 eV/atom, which compare to the present 0.58 eV/atom.

The cohesive energy is the energy required to separate an equilibrium solid into its constituent, isolated atoms at 0 K. While such data are available for the elements,[58] only measurements of the 298-K heat of formation ΔH_f^{298} are available for the silicides.[63–66] The heat of formation at 0 K may be written

$$\Delta H_f^0(\mathrm{Mo}_m\mathrm{Si}_n) = \frac{m}{m+n}E_{\rm coh}(\mathrm{Mo}) + \frac{n}{m+n}E_{\rm coh}(\mathrm{Si}) - E_{\rm coh}(\mathrm{Mo}_m\mathrm{Si}_n)\ , \quad (3)$$

while the expression for ΔH_f^T requires thermal corrections to each of the solid-phase energies entering the three cohesive energies on the right hand side of this equation. We suggest that $\Delta H_f^{298} - \Delta H_f^0 \sim 0.01$ eV/atom for $MoSi_2$,[61] and on this basis have combined ΔH_f^{298} data for the silicides with $E_{\rm coh}$ data for the elements in arriving via Eq. (3) at our "$T = 0$" experimental silicide cohesive energies in Table III. We have used the values suggested by Chart.[64] If references in recent compilations[65,66] are traced, his data appear not only to be more recent, but in addition the author has subjected his and other data from the literature to a consistency analysis, in arriving at what he claims to be the most reliable thermodynamic data for the molybdenum silicides at that time (1974).[64] These ΔH_f^{298} values (the dashed line in Fig. 4) are generally among the largest in magnitude cited for the silicides,[63–66] and also in closest agreement with the present $T = 0$ theoretical results obtained from Eq. (3), as may be seen in Fig. 4.

LDA cohesive energies are typically overbound, as is the case here by $\sim$ 0.8 eV/atom for the four metals, and 0.55 eV/atom for Si. The gradient correction to $E_{\rm coh}$ is monotonic across the series, overcorrecting by 0.6 eV/atom at the Mo end, while providing excellent agreement with experiment for $MoSi_2$ and Si as seen in Table III. The calculated DOS at the Fermi level also generally decreases across the series, and the value for $C11_b$ $MoSi_2$ is quite small, while Si is of course semiconducting. The LMH gradient correction to $E_{\rm coh}$ is thus best close to the insulating limit, in the case of the present series. Nevertheless, the $E_{\rm coh}$ errors more nearly cancel in the LDA ΔH_f values, which are seen in Fig. 4 to be in better agreement with the data. Note that cancellations between the cohesive energies of the individual silicides, Mo, and Si also make ΔH_f an order of magnitude smaller than these component energies, which greatly amplifies percentage errors in ΔH_f. All theoretical points in Fig. 4, except for the LDA+LMH A15 value, however, lie at concave-up intersections of the connecting line segments, consistent with thermodynamic stability. The crossing of the LDA and LDA+LMH curves at the $D8_m$ structure in this figure is accidental.

The calculated LDA V_0 values in Table III and Fig. 5 are 2.4–3.3% smaller than experiment for the four metals with these differences roughly halved by use of the gradient correction. Much of the remaining discrepancy between the LDA+LMH results and experiment seen in Table III and Fig. 5 for these metals may well be due to $\sim$1% lattice vibrational corrections.[62]

Except for $MoSi_2$, the LMH correction is seen in Table III to reduce the calculated values of B_0, as has been found for other gradient corrections.[67] Note, however, that all theoretical $E_{\rm coh}$ and B_0 values in this table have been evaluated at the respective theoretical V_0's, which are different for LDA and LDA+LMH. While our $E_{\rm coh}$ results change by less than 0.01 eV/atom if calculated at the experimental V_0's, the corresponding values for B_0 are noticeably changed. They are 258.0, 223.8, 230.8, 201.1, and 90.4 GPa for the LDA case; and 266.3, 233.9, 238.5, 214.1, and 96.1 GPa for the LDA+LMH case, where the order is A2, A15, ..., A4, respectively. The

LMH gradient correction is therefore seen to increase B_0 when calculated *at fixed volume*, as has also been found elsewhere for this and other gradient corrections.[55] Evidently, the LMH tendency to increase B_0 at fixed volume competes with a reduction in B_0 brought about by the larger LDA+LMH value of V_0, when calculations are performed at the theoretical equilibrium volume. This may explain the nearly unchanged LDA+LMH value of B_0 for $MoSi_2$ in Table III, since this phase exhibits the smallest LMH increase in V_0.

Our intention here is neither to survey possible gradient corrections, nor to test the most modern options,[68] but rather simply to make contact with one representative and tested candidate in order to provide a context for the present application. Our results are in fact quite consistent with the behavior found for other gradient corrections.[67] Specifically, we find significantly improved agreement with experiment for both E_{coh} and V_0, with some overcorrection of E_{coh} for Mo and of V_0 for Si, similar to other tests for Nb and Si, respectively.[67]

Finally, we note that the $C11_b$ disilicide stands out by having the most negative heat of formation in Fig. 4, and the smallest equilibrium volume per atom in Fig. 5. We believe these features to be associated with dominance of Mo-Si bonding in the disilicide. If so, the behavior of V_0 in Fig. 5 may be simply understood by considering each of the $A2$, $C11_b$, and $A4$ phases as effectively end members in regard to dominance of the three types of bonding, Mo-Mo, Mo-Si, and Si-Si, respectively. Differences between Mo-Mo and Mo-Si bonding are then smoothly interpolated by intermediate phases of mixed character in the four structure $A2$-$A15$-$D8_m$-$C11_b$ sequence, while entirely different Si-Si bonding is reflected in the final $A4$ phase.

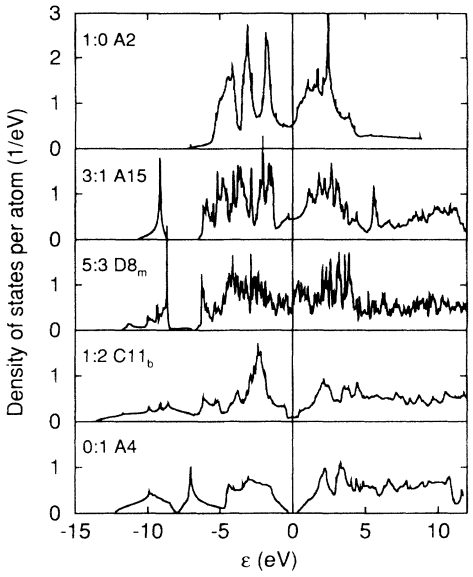

FIG. 6. Density of states for the five member Mo-Si series. The Fermi level is taken as the zero of energy.

V. DENSITY OF STATES

In this section, we examine the total DOS's for the molybdenum silicides, as well as their separate Si($3s$), Si($3p$), and Mo($4d$) contributions. Figure 6 presents the total DOS, $D(\varepsilon)$, obtained for the five member Mo/Si series using the full multiple-κ basis set, where here and throughout this paper the Fermi level, ε_F, is taken as the zero of energy for one-electron eigenvalues. We have divided by the total number of atoms irrespective of type, so that the integrated areas up to the Fermi level in Fig. 6 are 6, 5.5, 5.25, 4.67, and 4 electrons for Mo, Mo_3Si, Mo_5Si_3, $MoSi_2$, and Si, respectively. The densities of states at the Fermi level, $D(\varepsilon_F)$, are (top to bottom) 0.52, 0.45, 0.61, 0.09, and 0 states/eV for these $A2$, $A15$, $D8_m$, $C11_b$, and $A4$ phases, respectively. These values generally decrease with Si concentration, except for the $D8_m$ case. That value, however, might change on optimization of the four $D8_m$ internal parameters. As mentioned in Sec. IV, the gradient correction is best at the Si-rich end, which may correlate with this trend. Also note in Fig. 6 that the Fermi level is consistently found in a relatively pronounced dip in $D(\varepsilon)$, which reduces the band structure energy (sum of the occupied one-electron eigenvalues), and often correlates with structural stability.

More detailed insight is provided by Fig. 7, where separate Mo($4d$), Si($3s$), and Si($3p$) contributions to $D(\varepsilon)$ are shown by the solid, dotted, and dashed curves, respectively, obtained using our single-κ basis set. The low-lying Si($3s$) density (dotted curves) is quite evident in Fig. 7 in the vicinity of of $\varepsilon \sim -10$ eV. The predominantly Si($3s$) bands are completely separated from the higher-lying levels in the $A15$ and $D8_m$ cases, while an examination of high-symmetry levels suggests the anal-

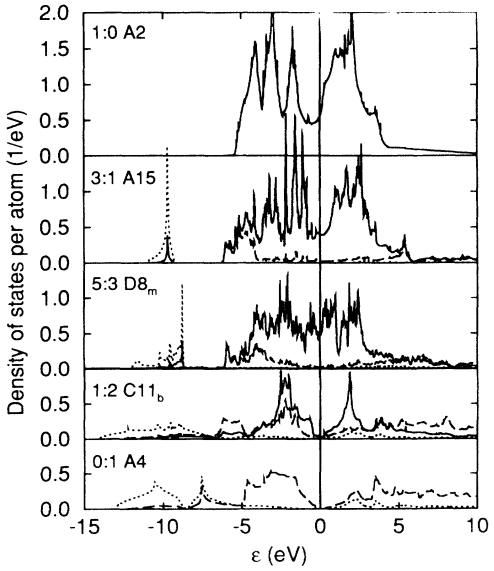

FIG. 7. Si($3s$) (dotted), Si($3p$) (dashed), and Mo($4d$) (solid) contributions to the DOS for the five member Mo-Si series. The zero of energy is the Fermi level.

ogous $C11_b$ bands range from -14 to about -3.5 eV in that case. The Mo($4d$) state density (solid curves) is seen to be roughly symmetrically distributed about ε_F in Fig. 7, with occupied states accounting for 50±3% of the total possible number of $4d$ electrons. The corresponding Si($3p$) percentages are 37±3% except for the A15 case (54%). These percentages are consistent with our suggestion in this work that the Mo($4d$) site energy, ε_d, lies close to ε_F throughout the series, while the corresponding Si($3p$) energy, ε_p, lies higher, at least for the $D8_m$ and $C11_b$ phases.

One striking aspect of the Mo-rich silicides ($A15$ and $D8_m$) in Fig. 7 is the close match between Mo($4d$) and Si($3p$) partial densities at the extremities of the predominantly Mo($4d$) regions, from about -6.2 to -5 eV, and again from about 5 to 10 eV in both phases, suggesting the crucial role of pd hybridization in these areas. The Si($3p$) states in the $A15$ structure are known to couple strongly with transition-metal dd bonding combinations.[42] The dd interactions alone place levels as low as -4.49 eV, judging from a Γ_1 state (93% Mo d and 7% Mo s) at this energy, which has bonding $d_{3x^2-r^2}$, $d_{3y^2-r^2}$, and $d_{3z^2-r^2}$ orbitals running along the near-neighbor Mo-Mo chains in the three respective directions. Additional pd interaction pushes some of these states to even lower energies as seen for the $A15$ phase in Fig. 7, and creates the small peak just above 5 eV, which our Mulliken overlap analysis shows to be pd antibonding, yet dd bonding, in agreement with earlier discussion.[42] We have not carried out detailed examination of the $D8_m$ case; however, both structural similarities and those between the $A15$ and $D8_m$ curves in Fig. 7 suggest similar behavior.

Another interesting characteristic of the Si($3p$) partial state densities for the $A15$ and $D8_m$ phases in Fig. 7, is the rather thorough separation between bonding and antibonding pd regions. Such segregation is a characteristic of covalency,[69] and is more pronounced here than observed in earlier surveys using high-symmetry structures.[30–32] This is a reminder of the crucial interplay between structure and bonding, e.g., fcc Si would be, and most likely is at high pressure,[70] an excellent free-electron metal.[71]

The most notable feature of the Si-rich $C11_b$ disilicide in Fig. 6 is its low $D(\varepsilon_F)$, which is suggestive of a hybridization gap. The major contributions to the peaks on either side of ε_F for this case are seen in Fig. 7 to come from Mo($4d$), and for the lower peak, also Si($3p$) components. The $C11_b$ disilicide has essentially identical near neighbor Mo-Si and Si-Si distances, without any particularly close Mo-Mo links. The obvious question is then which of these bond types, if not both, is responsible for the low $D(\varepsilon_F)$.

We suggest that the near hybridization gap at ε_F in $C11_b$ $MoSi_2$ is due exclusively to pd hybridization, i.e., Mo-Si bonds. First, we have transformed the one-electron Hamiltonian to a basis of numerical Wannier functions, using techniques described elsewhere,[72] and found that the hybridization gap persists when all near-neighbor Si-Si couplings are removed, but disappears entirely when the Mo-Si couplings are severed. Second, we find that a near-neighbor tight-binding treatment of the $C11_b$ structure in which only Mo(d)-Si(p) interactions are incorporated yields an insulating gap in the interval from ε_d to ε_p, with the state density symmetric about $(\varepsilon_d+\varepsilon_p)/2$, except for a δ function of area two (including spin degeneracy) at ε_p. The δ function arises from the fact that at every $\mathbf{k}$ point in the Brillouin zone, at least one of the six possible Si(p) molecular orbitals (two Si atoms per primitive cell × 3 orbitals) does not couple with the Mo(d) states.

The last point explains the counting for the Cr-group disilicides: 10 d + 12 p states per formula unit form ten fully occupied pd bonding states, with ten empty pd antibonding states lying at higher energies, and two empty pure-p noncoupling states also lying at higher energies. Other interactions and hybridizing components rearrange these states somewhat, leading to the small state density at ε_F seen for the $C11_b$ phase in Figs. 6 and 7. The $C40$ stacking variant, however, is known to be semiconducting for $CrSi_2$.[38]

VI. CHARGE DENSITY

In this section, we examine the valence charge density, $\rho(\mathbf{r})$, for the five member series in order to compare the relative buildup of charge density in the various types of bonds, and to assess the directional anisotropy of $\rho(\mathbf{r})$ in the vicinity of different sites. Both diagnostics consistently point to preferential accumulation of charge density in Mo-Mo, Mo-Si, and Si-Si bonds ordered from most to least favored. These differences are largely absent from superposed free atom electron densities, and so we judge them to be true reflections of the formation of bonds in the molybdenum silicides.

Locations, $\mathbf{r}$, at which we investigate the charge density are illustrated in Fig. 8, where $\rho(\mathbf{r})$ is plotted along one $\mathbf{z}$-

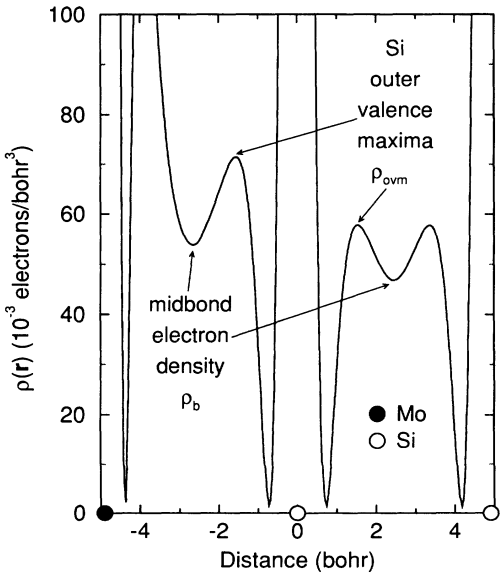

FIG. 8. Valence charge density along one $\mathbf{z}$-direction Mo-Si-Si chain in $C11_b$ $MoSi_2$, illustrating midbond electron densities, ρ_b, and Si outer valence maxima, $\rho_{ovm}(\hat{\mathbf{r}})$.

direction Mo-Si-Si chain for $C11_b$ $MoSi_2$. The "midbond electron densities," ρ_b, are the local extrema (usually minima) which occur near the midpoints of straight line paths between the two neighbors under consideration. Due to nodes in the Si($3sp$) and Mo($4d$) wave functions, there are also atomiclike local maxima in $\rho(\mathbf{r})$ which occur at distances of ~1.5 and ~ 1.0 bohr from each Si and Mo atom, respectively. In contrast to the midbond minima, ρ_b, these "outer valence maxima," $\rho_{\rm ovm}(\hat{\mathbf{r}})$, provide an atom-specific diagnostic of local anisotropy about a given site (taken for convenience at $\mathbf{r}=0$), which is not dependent on near-neighbor distances.

In the remainder of this section, we report our calculated values of ρ_b, and then present a site-by-site survey of $\rho_{\rm ovm}(\hat{\mathbf{r}})$ anisotropy. Note that all charge densities reported here and throughout this paper were obtained with highly accurate multiple-κ calculations, and that in particular, the diffuse Si($3sp$) orbitals are each expanded in three augmented Hankel functions with decay energies $-\kappa^2 = -0.01$, -1, and -2.3 Ry. The valence charge density results presented here generally exclude Mo($4sp$) semicore states [Fig. 8, all ρ_b values and $\rho(\mathbf{r})$ contour plots]. However, semicore contributions to the Si $\rho_{\rm ovm}(\hat{\mathbf{r}})$ are not only small, but they largely cancel out anisotropic differences, $\rho_{\rm ovm}^{\rm max} - \rho_{\rm ovm}^{\rm min}$, as well as differences, $\Delta\rho_{\rm ovm}(\hat{\mathbf{r}})$, between self-consistent and superposed free-atom densities for the Mo sites. In these cases [all $\rho_{\rm ovm}^{\rm max} - \rho_{\rm ovm}^{\rm min}$ and $\Delta\rho_{\rm ovm}(\hat{\mathbf{r}})$ values] we cite valence density results, obtained in an earlier stage of this work, which include the semicore contributions.

A. Midbond charge density

Figure 9(a) presents our results for the midbond valence electron densities, ρ_b, for all bonds shorter than 5.6 bohr in the five member series. The excluded Mo($4sp$) semicore states would roughly double the separations between these curves, were they included. The difference, $\Delta\rho_b$, between self-consistent and superposed free-atom densities is shown in Fig. 9(b), where Mo($5s^2 4d^4$) and Si($3s^2 3p^2$) atom configurations were taken. Changing the Mo atom configuration to $5s^1 4d^5$ has small impact, raising these $\Delta\rho_b$ curves by ~2 millielectrons/bohr^3 at the larger bond lengths.

Both ρ_b and $\Delta\rho_b$ values in Fig. 9 suggest a systematic hierarchy of charge density in silicide bonds of the same length, namely, Mo-Mo, Mo-Si, and Si-Si in order of greatest to least bond density. The separations between the curves in Fig. 9(a) and those in 9(b) are roughly comparable due to the fact that differences between values of ρ_b as obtained from the superposed free-atom electron densities are a factor of three or more smaller for the three bond types than those seen in Fig. 9(a). The relative midbond densities in Fig. 9(a), therefore, appear to be a true consequence of preferential self-consistent accumulation of electron density in certain bonds, rather than being due to systematic differences in the size of Mo($4d$) versus Si($3p$) orbitals in the midbond region. Since the free-atom superposition is intrinsically limited to orbital contributions of the form $|\phi_a(\mathbf{r})|^2$, one obvious candidate

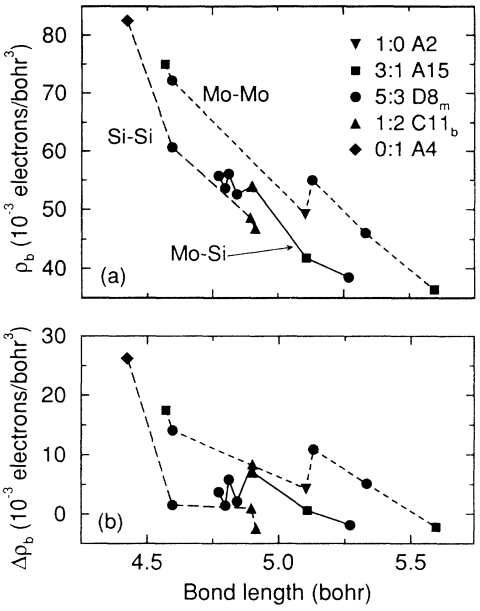

FIG. 9. Midbond valence charge densities for the five member Mo-Si series: (a) self-consistent values, ρ_b, and (b) differences, $\Delta\rho_b$, between self-consistent and superposed free-atom values.

for providing some of this enhancement is the significant appearance in the self-consistent charge density of bonding cross terms $\mathrm{Re}[\phi_a(\mathbf{r})^*\phi_b(\mathbf{r})]$, whose cumulative weight is measured by integrals of the appropriate off-diagonal Mulliken state densities, as will be discussed in Sec. VII.

B. Survey of site anisotropy

Table IV gives the difference, $\rho_{\rm ovm}^{\rm max} - \rho_{\rm ovm}^{\rm min}$, between maximum and minimum values of $\rho_{\rm ovm}(\hat{\mathbf{r}})$ as a function of direction, $\hat{\mathbf{r}}$, for all inequivalent Si and Mo sites in the five structure series. The $A15$ and $D8_m$-a Si sites are both seen to be relatively isotropic. Isotropy of the high-symmetry $A15$ Si site, which has 12 Mo near neighbors, is not surprising. The $D8_m$-a site, on the other hand, has two Si near neighbors in the $\pm\mathbf{z}$ directions, as seen in Fig. 2(b), and eight Mo k second neighbors which are 5% more distant. Its $\rho_{\rm ovm}(\hat{\mathbf{r}})$ isotropy results from a self-consistent reduction which is largest ($\Delta\rho_{\rm ovm} = -6.4$ millielectrons/bohr^3) in the near-neighbor directions, and smallest ($\Delta\rho_{\rm ovm} = -2.2$ millielectrons/bohr^3) in the $\mathbf{x}$,$\mathbf{y}$ plane, clearly a compromise response to all eight of the Mo neighbors. Figure 9(b) also shows a slightly larger self-consistent enhancement of the second neighbor Si-Mo midbond valence density than for the first neighbor Si-Si bond. Therefore, the very isotropy of the $D8_m$-a Si $\rho_{\rm ovm}(\hat{\mathbf{r}})$ is a reflection of the enhancement of the second neighbor Mo-Si bonds at the expense of the 5% shorter Si-Si bonds.

Table IV shows dramatically larger anisotropy for the lower-symmetry $D8_m$-h Si site, which has six close Mo neighbors (two each at d = 4.77, 4.80, and 4.81 bohr).

TABLE IV. Anisotropy of the valence charge density ρ near Mo and Si atoms in the Mo/Si structures. Here ρ_{ovm} is the local maximum (outer valence maximum) of ρ which occurs ~ 1.5 bohr from each Si atom, and ~ 1.0 bohr from each Mo atom. The extent of the directional variation $\rho_{ovm}^{max} - \rho_{ovm}^{min}$ is specified (in 10^{-3} electrons/bohr^3), as well as the Wyckoff site letter and the site symmetry.

Structure	Compound	Si			Mo		
		$\rho_{ovm}^{max} - \rho_{ovm}^{min}$	site	symmetry	$\rho_{ovm}^{max} - \rho_{ovm}^{min}$	site	symmetry
$A2$	Mo				48.1	a	O_h
$A15$	Mo_3Si	1.8	a	T_h	37.4	c	D_{2d}
$D8_m$	Mo_5Si_3	3.1	a	D_4	36.0	b	D_{2d}
		17.6	h	C_{2v}	48.4	k	C_{1h}
$C11_b$	$MoSi_2$	17.7	e	C_{4v}	41.6	a	D_{4h}
$A4$	Si	37.7	a	T_d			

Figure 10 shows the valence charge density contours for part of the cross section shown in Fig. 1(c). The directional local maxima of $\rho_{ovm}(\hat{\mathbf{r}})$ for the lower-center Si h atom in Fig. 10 lie within the two crescent shaped contours above and below this site. These point towards the midpoints of Mo-Mo pairs, both above (first k and second b neighbors, the latter lie above and below the plane of the paper, with their midpoint halfway between the two Si h sites), and below (third k neighbors). Similarly, the most positive $\Delta\rho_{ovm}$ and $\Delta\rho_b$ values occur in the direction of these first six Mo neighbors, while the most depleted directions lie out of the plane of the paper and down (away from the second b neighbors).

In spite of the essentially identical coordination of five Si and five Mo atoms about each Si site in the $C11_b$ disilicide, as seen in Fig. 2(d), both the magnitude and self-consistent response of the valence charge density unequivocally identify the Si-Mo bonds as being stronger. The midbond densities, ρ_b, for example, are 20–30% larger for the Si-Mo bonds, mostly due to self-consistent response, as can be seen in Fig. 9. The Si $\rho_{ovm}(\hat{\mathbf{r}})$ anisotropy is evident from Fig. 11, which gives valence electron density contours for the (110) cross section of Fig. 1(g). Local maxima of $\rho_{ovm}(\hat{\mathbf{r}})$ are in the directions of neighboring Mo atoms, and lie within the crescent shaped contours about each Si site. Values of $\rho_{ovm}(\hat{\mathbf{r}})$ are 71.8 and 66.3 millielectrons/bohr^3 for **z** and lateral directions, respectively. The corresponding back bond (Si direction) values are 57.9 and 59.7 millielectrons/bohr^3, respectively. This anisotropy is due almost exclusively to self-consistent response of the valence charge density, since the superposed atom calculation of $\rho_{ovm}(\hat{\mathbf{r}})$ is con-

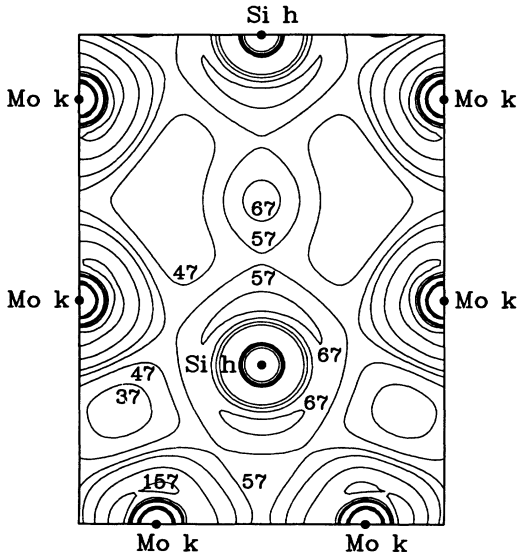

FIG. 10. Valence charge density contours for $D8_m$ Mo_5Si_3. Part of the cross section in Fig. 1(c) is shown. Directional local maxima in the Si $\rho_{ovm}(\hat{\mathbf{r}})$ lie in the crescent shaped contours below and above each Si h site. Contours shown are 37, 47, 57, 67, 97, and 157 millielectrons/bohr^3.

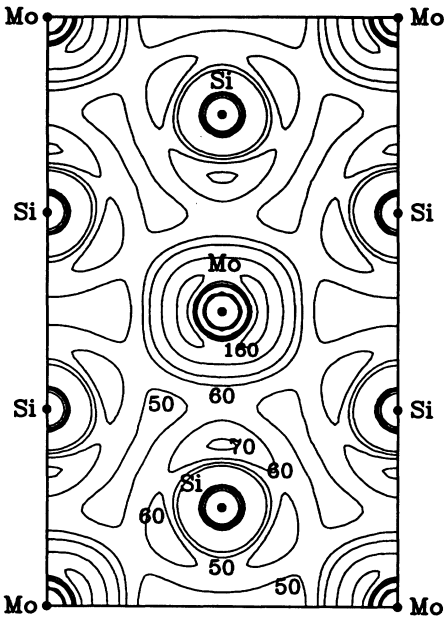

FIG. 11. Valence charge density contours for $C11_b$ $MoSi_2$. The cross section in Fig. 1(g) is shown. Directional local maxima in both Si and Mo $\rho_{ovm}(\hat{\mathbf{r}})$ lie in the crescent shaped contours close to each such site. Contours shown are 40, 50, 60, 70, 100, and 160 millielectrons/bohr^3. The corresponding plot of $\rho(\mathbf{r})$ along the vertical -Mo-Si-Si- chains is shown in Fig. 8.

stant to within about ± 1 millielectrons/bohr^3.

The Si $\rho_{\rm ovm}(\hat{\mathbf{r}})$ values just cited also attest to the inequivalence of the two Si-Mo bonds in $C11_b$ $MoSi_2$. Not only does the **z**-direction Si-Mo bond exhibit greater buildup of charge density, but it is the most directional in the sense that $\rho_{\rm ovm}(\hat{\mathbf{r}}) - \rho_{\rm ovm}^{\rm min}$ decreases by at least a factor of three for all directions away from **z**. The four lateral bonds from each Si to neighboring Mo atoms, on the other hand, are separated as a function of direction, $\hat{\mathbf{r}}$, by saddle points where $\rho_{\rm ovm}(\hat{\mathbf{r}}) - \rho_{\rm ovm}^{\rm min}$ decreases by only $\sim$20%. This suggests more metallic character for these bonds, and reduced angular rigidity.

For completeness, we have also examined the Mo $\rho_{\rm ovm}(\hat{\mathbf{r}})$, which are seen from Table IV to exhibit a rather uniform degree of anisotropy across the molybdenum silicide series. Maxima generally occur in near-neighbor directions, switching from Mo to Si neighbors as these become closer in progressing across the series. The only surprising case is the $C11_b$ Mo site which exhibits a pronounced T_{2g}-like anisotropy favoring its eight lateral Si neighbors at the corners of the slightly squashed cube in Fig. 2(c), at the expense of the two **z**-direction near neighbors. This anisotropy has been previously noted by Mattheiss,[38] is evident in the contour plot of Fig. 11, and becomes less visible if Mo($4p$) contributions are included in the valence charge density.[36] Since the midbond densities for the lateral and **z**-direction Mo-Si bonds are nearly the same [the symbols overlap in Fig. 9(a)], the combined anisotropies in Fig. 11 suggest a greater Mo contribution to the former, and Si contribution to the latter bonds.

VII. TIGHT-BINDING/MULLIKEN ANALYSIS

We demonstrate here a systematic $\sim$5 eV offset between Si($3p$) and Mo($4d$) site energies across the molybdenum silicide series, which we believe to be the underlying cause of the bond hierarchy addressed in this paper. After giving a brief overview of the combined tight-binding and Mulliken[46] analysis used in this section, we describe our calculation of the site energies. Then we show off-diagonal Mulliken functions for selected bonds in order to illustrate the relationship between site energies and electron densities.

A. Overview of the analysis

For simplicity, we prefer an orthogonal orbital basis for the tight-binding perspective, i.e., Eq. (2). A useful Mulliken treatment for such a basis requires removal of the overlap matrix elements from the standard definitions[46] of the partial state densities, $D_{qq'}(\varepsilon)$, where $q \equiv \mathbf{q}nlm$ is an abbreviation for atomic basis site, principal, angular, and magnetic quantum numbers. The virtue of such a modified Mulliken analysis, as discussed in the Appendix, is that tight-binding site energies, ε_q, and hopping parameters, $t_{qq'}$, are then simply related to the diagonal, $D_{qq}(\varepsilon)$, and off-diagonal, $D_{qq'}(\varepsilon)$, partial state densities, respectively. Moreover, the charge density, $\rho(\mathbf{r},\varepsilon)$, may be simply expressed in terms of orbital products $\phi_q(\mathbf{r})\phi_{q'}(\mathbf{r})$ and integrals, $N_{qq'}(\varepsilon)$, of the partial state densities, $D_{qq'}(\varepsilon)$.

$$\rho(\mathbf{r},\varepsilon) = \sum_{qq'} N_{qq'}(\varepsilon)\,\phi_q(\mathbf{r})\,\phi_{q'}(\mathbf{r}). \tag{4}$$

We consider the valence charge density accumulated up to a general energy, ε, take the orbitals $\phi_q(\mathbf{r})$ to be real, and take a large enough set of atomic basis sites so that only orbitals associated with Bravais lattice vector $\mathbf{R}=0$ are important near $\mathbf{r}$.

The connection between tight-binding parameters and electron densities is made through the integrals $N_{qq'}(\varepsilon)$ evaluated at the Fermi level, $\varepsilon = 0$. These partial state number functions show bonding and antibonding state density by regions of positive and negative slope, respectively, and their areas are exactly the $t_{qq'}$ (See Appendix). The distribution in energy, ε, of qq' bonding state density is determined by the site energies ε_q and $\varepsilon_{q'}$, by $t_{qq'}$, and by other hybridizing influences (e.g., $t_{qq''}$ and $t_{q'q''}$). We suggest that the hierarchy in midbond electron densities documented in the previous section coincides with differing net accumulations of bonding density, which is in turn ultimately due to the Si($3p$)-Mo($4d$) site energy differences $\varepsilon_p - \varepsilon_d$.

We have not calculated the orthogonal orbitals $\phi_q(\mathbf{r})$ corresponding to $H_{\rm or}$ of Eq. (2); however, we believe the orbital products in Eq. (4) are unlikely to explain the trends in Fig. 9. First, the nonorthogonal Si $3p_z$ augmented Hankel functions, for example, are generally larger throughout the important 2.2–2.8 bohr midbond range than are the corresponding Mo $4d_{3z^2-r^2}$ functions (all with -0.5 Ry decay energies), which is contrary to the trends in Fig. 9. Second, we have noted that superposed free atom electron densities show dramatically (factor of three or more) reduced differences between the three types of bonds, suggesting at least that generic properties of Mo($4d$) and Si($3p$) orbitals are not responsible for the offsets in Fig. 9. Finally, as described below, we find significant correlation both in size and energy dependence of the midbond $\rho(\mathbf{r},\varepsilon)$ with relevant functions $N_{qq'}(\varepsilon)$.

B. Site energies

Figure 12 shows site energies, ε_q, obtained from the $H_{\rm or}$ using Eq. (A6), where in each case averages over the magnetic quantum number, m, have been performed, and the resultant energies are given relative to the FP-LMTO Fermi levels. The data points show the values actually obtained for the various structures, while the curves are guides to the eye. There are two sets each of Mo and Si values for the $D8_m$ phase at $x=0.375$, corresponding to the various inequivalent sites. We believe these results to be representative of the molybdenum silicides as described by localized orthonormal bases. As an indication of potential variability in such descriptions, the $C11_b$ values at $x=0.67$ in Fig. 12 are -1.9, 1.0, 5.7, 13.9, and 17.5 eV, while a numerical generation[72] of orthogonal Wannier functions yields -2.9, 2.1, 5.2, 10.8, and 14.8 eV,

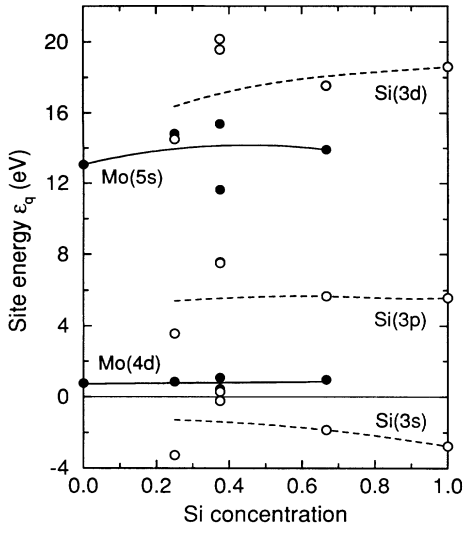

FIG. 12. Site energies corresponding to the localized, orthogonal basis in which Eq. (2) is defined. Values calculated from Eq. (A6) are indicated by data points, while the curves are guides to the eye. The FP-LMTO Fermi level is the zero of energy.

where the order is Si($3s$), Mo($4d$), Si($3p$), Mo($5s$), and Si($3d$), respectively. The agreement is ~ 1 eV, or for the higher lying energies, $\sim$30%. Note that nonorthogonal-basis site energies are quite different. The Si($3s$) site energies corresponding to the present augmented Hankel functions (-0.5 Ry decay energies) are ~ -9 eV, for example, while the Mo($4d$) and Si($3p$) site energies lie within $\sim$1.5 eV of one another. Orthogonalization shifts are positive, and largest for the smaller angular momenta, consistent with the effects of the distortion or nonorthogonality parameters, γ_l, in LMTO theory.[51,52]

While adequate for our present purposes, the tight-binding characterizations in Fig. 12 exhibit larger site-energy scatter as a function of Si concentration than would be optimal for a transferable representation of the molybdenum silicide series as a whole. Orthogonalization shifts are not the main cause of this scatter, since we also find significant scatter in the nonorthogonal augmented Hankel function site energies. Rather we believe much of this variation reflects differences in the muffin-tin radii, which could be adjusted to reduce the scatter. This conclusion is based on the fact that LMTO band centers,[51,52] which are site energies for muffin-tin orbitals defined by similar boundary conditions at the muffin-tin radii, fall on stoichiometry-independent curves when the combined values for all five materials are plotted as a function of muffin-tin radius. Finally, note that we did not include basis orbitals in the interstitial spheres when calculating the $A4$ Si site energies in Fig. 12, making this tight-binding representation less accurate than those for the more close-packed metals. Nevertheless, the $x = 1$ Si values in Fig. 12 are reasonably consistent with those suggested by other orthogonal tight-binding characterizations for this material.[69]

C. Mulliken analysis

Figure 13 considers the first Mo-Mo (solid curves) and second Mo-Si (dashed curves) neighbor bonds in $A15$ Mo_3Si, where the geometry may be seen in Fig. 2(a). The upper two panels of Fig. 13 show the $N_{qq'}(\varepsilon)$ for neighboring $d_{3z^2-r^2}$–$d_{3z^2-r^2}$ and d_{zx}–p_z pairs of orbitals, respectively. To better expose the underlying effect of the site energies, Fig. 13(a) shows $N_{qq'}(\varepsilon)$ curves for relatively "pure" $t_{qq'}$ interactions, i.e., with most other hybridizing influences $t_{qq''}$ and $t_{q'q''}$ set to zero. This was achieved by working with submatrices of H_{or} which retained only Mo($4d$) and Si($3p$) components and in addition by setting intersite pd (Mo-Mo case) or dd (Mo-Si case) couplings to zero. Figure 13(b) shows the full $N_{qq'}(\varepsilon)$ curves with all couplings. The corresponding FP-LMTO midbond charge density $\rho(\mathbf{r}_b, \varepsilon)$ is given as a function of energy for the Mo-Mo and Mo-Si cases by the filled circles with connecting solid line, and by the open circles with connecting dashed line, respectively, in Fig. 13(c). A scaled version of the DOS, $D(\varepsilon)$, is provided for reference.

For the pure interaction case in Fig. 13(a), the bonding (positive slope) and antibonding (negative slope) states are seen to be roughly symmetrically disposed about ε_d for dd interactions, and about $\frac{1}{2}(\varepsilon_d + \varepsilon_p)$ for pd interactions. The areas of these curves are the appropriate hop-

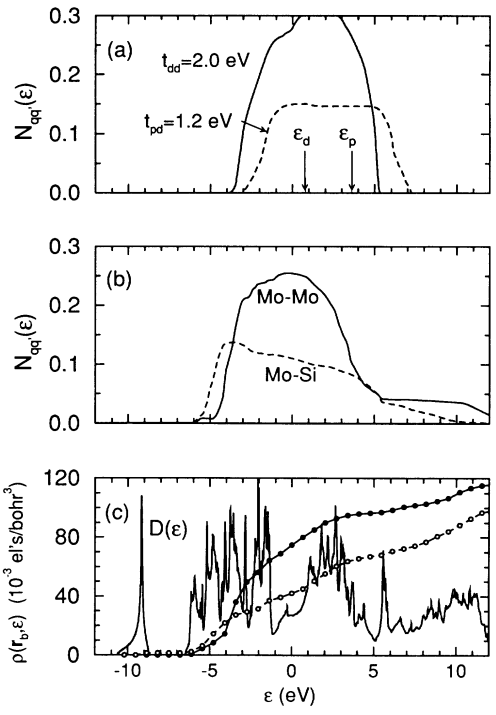

FIG. 13. Mulliken analysis of first Mo-Mo (solid curves) and second Mo-Si (dashed curves) neighbor midbond electron densities $\rho(\mathbf{r}_b, \varepsilon)$ in $A15$ Mo_3Si. (a) Off-diagonal number of states functions $N_{qq'}(\varepsilon)$ for orbital pairs q and q' with primarily only $t_{qq'}$ interactions. (b) The same with all interactions. (c) FP-LMTO calculated $\rho(\mathbf{r}_b, \varepsilon)$ for Mo-Mo (filled symbols) and Mo-Si (open symbols), with the scaled $D(\varepsilon)$ given for reference.

ping parameter magnitudes, as noted in the Appendix. Here, $t_{dd} = -V_{dd\sigma}$ and $t_{pd} = -0.743\,V_{pd\sigma}$, taking Harrison's $V_{pd\pi}/V_{pd\sigma}$ ratio.[69] Figure 13(a) suggests that longer bonds accumulate less electron density not only due to smaller midbond orbital products $\phi_q(\mathbf{r}_b)\,\phi_{q'}(\mathbf{r}_b)$, but also due to their smaller interactions $t_{qq'}$, which tend to correlate with smaller values of $N_{qq'}(\varepsilon)$. The overall size of $N_{qq'}(\varepsilon)$ is further reduced for the pd case due to the different site energies which further spread out the area t_{pd}. This is consistent with the Mo-Si ρ_b values in Fig. 9(a) lying somewhat below the average of the Mo-Mo and Si-Si values. When all hybridization couplings are present, Fig. 13(b), the areas under the two $N_{qq'}(\varepsilon)$ curves are preserved; however, Mo $d_{3z^2-r^2}$, d_{zx}, and Si p_z state densities become spread over broader energy ranges, similarly decreasing the overall values of the $N_{qq'}(\varepsilon)$ functions at any given ε. Note that Fig. 13(b) shows a leading, lower edge of pd hybridization in agreement with the earlier discussion of the $A15$ results in Fig. 7, and consistent with the larger second neighbor Mo-Si $\rho(\mathbf{r}_b,\varepsilon)$ values in Fig. 13(c) near $\varepsilon \sim -5$ eV.

The FP-LMTO calculated $\rho(\mathbf{r}_b,\varepsilon)$ curves in Fig. 13(c) depend also on contributions from other orbital types, and on the diagonal terms in Eq. (4) as well. We estimate, for example, that about 60% of the Mo-Mo value of $\rho(\mathbf{r}_b,0)$ in Fig. 13(c) comes from $d_{3z^2-r^2}$–$d_{3z^2-r^2}$ overlaps, with most of the remainder involving Mo $5s$ or $5p_z$ orbitals on one or another of the two sites. The combined diagonal and off-diagonal terms for two near neighbor $d_{3z^2-r^2}$ orbitals yield a curve whose shape is very similar to the filled-circle curve in Fig. 13(c), except that it levels off above about 4 eV. In particular, contributions to the positive slope of the Mo-Mo curve in Fig. 13(c) at $\varepsilon = 0$ come from nonbonding d states which appear only in the diagonal Mulliken function. Such nonbonding d states near ε_F are characteristic of transition metal silicides.[30–32]

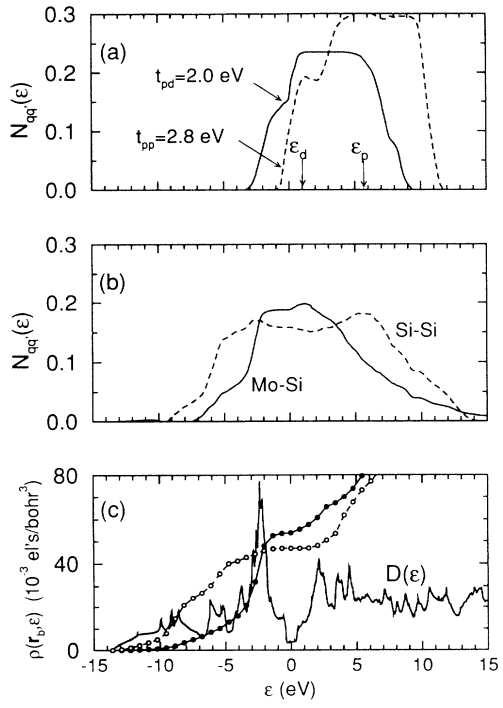

FIG. 14. Mulliken analysis of first neighbor Mo-Si (solid curves) and Si-Si (dashed curves) midbond electron densities $\rho(\mathbf{r}_b,\varepsilon)$ in $C11_b$ $MoSi_2$. (a) Off-diagonal number of states functions $N_{qq'}(\varepsilon)$ for orbital pairs q and q' with primarily only $t_{qq'}$ interactions. (b) The same with all interactions. (c) FP-LMTO calculated $\rho(\mathbf{r}_b,\varepsilon)$ for Mo-Si (filled symbols) and Si-Si (open symbols), with the scaled $D(\varepsilon)$ given for reference.

Figure 14 provides a comparable analysis of the **z**-direction first-neighbor Mo-Si (solid curves and filled circles) and Si-Si (dashed curves and open circles) bonds in the Si-rich $C11_b$ disilicide. This comparison is of particular interest since the two bond lengths are essentially identical, providing for even-handed competition. The neighboring orbital pairs considered in the $N_{qq'}(\varepsilon)$ calculations were $d_{3z^2-r^2}$–p_z and p_z–p_z, respectively, with these Mulliken calculations carried out for a doubled simple-tetragonal cell in order to isolate the **z**-direction bonds. Similar to the $A15$ case, the bonding and antibonding states for the pure couplings in Fig. 14(a) are roughly symmetrically disposed about $\frac{1}{2}(\varepsilon_d+\varepsilon_p)$ for the pd case, and about ε_p, for the the pp case. The areas indicated in Fig. 14(a) are $t_{pd} = -V_{pd\sigma}$ and $t_{pp} = V_{pp\sigma}$. It may be seen from this figure that the relative strength of Si-Si versus Mo-Si bonds is then a competition between the stronger Si-Si interaction ($t_{pp} > t_{pd}$), which favors the former, and the more optimal Mo($4d$) site-energy placement ($\varepsilon_F \sim \varepsilon_d < \varepsilon_p$), which favors the latter. This competition is complicated by the inclusion of all hybridization effects in Fig. 14(b), among which Mo $5s$, $5p$, and $4d$ admixtures are all instrumental in extending the Si-Si curve to lower energies (while preserving its area). Figure 14(b) is then consistent with the $\rho(\mathbf{r}_b,\varepsilon)$ results in Fig. 14(c), namely an initial low energy dominance of the Si-Si bond, which is overtaken near ε_F by the increase of charge density in the Mo-Si bond.

While it is not obvious that $\rho(\mathbf{r}_b,0)$ should end up actually being larger for the Mo-Si bond in Fig. 14(c), it seems clear for the molybdenum silicide series as a whole, that the relative site-energy positions ($\varepsilon_F \sim \varepsilon_d < \varepsilon_p$) are the most likely single factor favoring the general Mo-Mo, Mo-Si, and Si-Si hierarchy as seen in Fig. 9. Certainly the interaction strengths go as $|V_{dd\sigma}| < |V_{pd\sigma}| < |V_{pp\sigma}|$ for bonds of equal length,[73] which is contrary to the trend seen in the midbond charge density.

VIII. SUMMARY

We have reported *ab initio* local-density functional calculations of the bulk properties, DOS, and charge density for all room-temperature stable phases of the binary Mo-Si system. Our calculated densities of states for the three observed molybdenum silicide phases exhibit clear evidence of strong Mo($4d$)-Si($3p$) hybridization, in agreement with general expectations for the transition metal silicides.[23–43] The Mo-rich $A15$ Mo_3Si and $D8_m$ Mo_5Si_3 phases show pronounced bond-antibond separa-

tion in such hybrids, while we demonstrate that the low DOS at the Fermi level in $C11_b$ $MoSi_2$ is due to what is nearly a *pd* hybridization gap.

By using a method which makes no shape approximation to the one-electron potential,[44,45] we have been able to make quantitative comparisons of the valence charge density in all reasonably short bonds found in the three molybdenum silicides. We find a systematic hierarchy, Mo-Mo, Mo-Si, and Si-Si, in the order of greatest to least charge density in bonds of the same length. Directional anisotropy of the charge density in the vicinity of Si atoms also favors Mo over Si neighbors in a disproportionate manner, which is consistent with this hierarchy. These differences, which are dramatically reduced for superposed free-atom electron densities, appear to be a true reflection of relative bond strengths in the molybdenum silicides.

In order to better understand this behavior, we have carried out a modified Mulliken analysis in a reduced orthogonal basis, which facilitates simple tight-binding interpretation. Pronounced bond-antibond separation is observed for all *dd*, *pd*, and *pp* overlap densities that we have examined. We find, however, that while the Mo(4*d*) site energies, ε_d, are systematically close to the Fermi level, the Si(3*p*) site energies, ε_p, lie 5±2 eV higher for the three silicides. This suggests decreasing fractions of the *dd*, *pd*, and *pp* bonding states are occupied which we believe ultimately to be responsible for the above mentioned hierarchy. In spite of the large site energy difference, however, intersite couplings or hopping parameters are sufficiently large (bond-antibond splittings are typically 10 eV or larger) that the molybdenum silicides are still far more covalent than ionic.

These results imply an asymmetry in the Mo-Si phase diagram in which Mo-Mo bonds are favored at the Mo-rich side; yet Mo-Si bonds, at the Si-rich side. There is certainly ample reason to believe that Mo-Si bonding predominates in the Si-rich $C11_b$ disilicide: a near *pd* hybridization gap, significant differences in both midbond values and the directional anisotropy of the charge density, and the fact that there are twice as many Mo-Si as Si-Si bonds in this phase. The systematics of the equilibrium volume are then simply explained by an interpolation between dominant Mo-Mo and Mo-Si bonding throughout the $Mo\text{-}Mo_3Si\text{-}Mo_5Si_3\text{-}MoSi_2$ sequence, followed by an abrupt change to Si-Si bonding in pure Si. Similarly, since the heat of formation measures the difference, roughly speaking, between Mo-Si and some suitable average of the Mo-Mo and Si-Si interactions, it is not surprising that $C11_b$ $MoSi_2$ exhibits the largest $|\Delta H_f|$ of the molybdenum silicides.

Our analysis of the molybdenum silicides has identified the critical elements of the electronic structure in these materials. While this information is of intrinsic interest it also represents the first stage in our ultimate goal of providing a more realistic representation of the interatomic forces to be used in molecular dynamics simulations of Mo-Si interfaces. In particular, any accurate model must include the critical elements elucidated here. Among these, the bonding hierarchy, Mo-Mo, Mo-Si, Si-Si, already suggests a chemical component to the experimentally observed asymmetry between Mo-on-Si and Si-on-Mo interlayer thicknesses.[3] In the former case, adatom-substrate interactions are stronger than those between different substrate atoms, thereby enhancing diffusion of Mo into the Si substrate, whereas the reverse is true in the latter case, thereby impeding diffusion of Si into the Mo substrate. While empirical interatomic potentials may exhibit some of these characteristics,[20] our results provide a systematic and physically motivated basis upon which to include these chemical effects in improved representations of the interatomic forces in the binary Mo/Si system.

ACKNOWLEDGMENTS

This work was performed under the auspices of the U.S. Department of Energy by Lawrence Livermore National Laboratory under Contract No. W-7405-Eng-48. We gratefully acknowledge conversations with D. B. Boercker and P. E. A. Turchi.

APPENDIX

Mulliken decomposition of the one-electron DOS is an inherently nonunique, yet exceedingly valuable interpretive tool.[46] Convenient use of the present nonorthogonal augmented Hankel function basis to achieve such decomposition has already been discussed elsewhere.[56] Here we extend this discussion by noting interrelationships that exist between the Mulliken partial state densities and tight-binding parameters, when the Mulliken analysis is modified for use with an orthogonal basis.

For orthogonal bases, it is more convenient to define Mulliken partial state densities by expansion of the eigenvectors rather than eigenfunctions,

$$D_{qq'}(\varepsilon) = \frac{1}{N}\sum_k \delta(\varepsilon-\varepsilon_k)\ \mathrm{Re}[\alpha^*_{q'k}\alpha_{qk}]\ . \tag{A1}$$

Here, ε_k are the one-electron eigenvalues, and the one-electron eigenfunctions, $\psi^k(\mathbf{r})$, are given in terms of the basis orbitals, $\phi_q(\mathbf{r})$, or their Bloch sums, $\phi^{\mathbf{k}}_q(\mathbf{r})$, by

$$\psi^k(\mathbf{r}) = \sum_q \alpha_{qk}\frac{1}{\sqrt{N}}\sum_{\mathbf{R}} e^{i\mathbf{k}\cdot\mathbf{R}}\phi_q(\mathbf{r}-\mathbf{R}) = \sum_q \alpha_{qk}\,\phi^{\mathbf{k}}_q(\mathbf{r}). \tag{A2}$$

We abbreviate $k = \mathbf{k}j$ ($\mathbf{k}$ vector and band index) and $q = \mathbf{q}nlm$ (atomic basis vector, principal, angular, and magnetic quantum numbers). The customary definition[46,56] of the $D_{qq'}(\varepsilon)$ would include the overlap matrix element $\langle\phi^{\mathbf{k}}_{q'}|\phi^{\mathbf{k}}_q\rangle$ inside the square brackets in Eq. (A1), which is not useful for orthogonal orbitals where $\langle\phi^{\mathbf{k}}_{q'}|\phi^{\mathbf{k}}_q\rangle \propto \delta_{qq'}$.

While off-diagonal terms now no longer contribute to the total state density, i.e.,

$$D(\varepsilon) = \sum_q D_{qq}(\varepsilon)\ , \tag{A3}$$

they do contribute to the charge density, which for relatively localized orbitals is given by

$$\rho(\mathbf{r},\varepsilon) = \sum_{qq'} N_{qq'}(\varepsilon)\,\phi_q(\mathbf{r})\,\phi_{q'}(\mathbf{r}) \ . \tag{A4}$$

Here we generalize the usual charge density, $\rho(\mathbf{r},\varepsilon_F)$, by considering integrals up to energies other than the Fermi energy, ε_F; define partial number of states functions

$$N_{qq'}(\varepsilon) \equiv \int_{-\infty}^{\varepsilon} d\varepsilon'\, D_{qq'}(\varepsilon') \ ; \tag{A5}$$

and assume the orbital basis functions, $\phi_q(\mathbf{r})$, to be real. We also assume that $\mathbf{r}$ lies interior to the general region of the atomic basis sites $\{\mathbf{q}\}$, and that the basis has been taken large enough (using a supercell if necessary) so that orbitals $\phi_q(\mathbf{r}-\mathbf{R})$ associated with Bravais lattice vectors $\mathbf{R} \neq \mathbf{0}$ are unimportant at $\mathbf{r}$. The meaning of Eqs. (A3) and (A4) is that the off-diagonal terms here can add no new charge to the system, but do *redistribute* charge density. Bonding or antibonding character is then still related to the enhancement or depletion of charge density between neighboring atoms, which according to Eq. (A4) depends on the size and sign of the area under the relevant partial state densities, $D_{qq'}(\varepsilon)$, integrated up to the energy of interest. The net areas $N_{qq'}(\infty)$ are zero, i.e., there are equal amounts of bonding and antibonding state density.

The tight-binding connection follows from the fact that appropriate site energies, ε_q, for the orbital q, and hopping parameters, $t_{qq'}$, coupling different orbitals q and q' are given by

$$\varepsilon_q = \int_{-\infty}^{\infty} d\varepsilon\, \varepsilon\, D_{qq}(\varepsilon) \ , \tag{A6}$$

and

$$t_{qq'} = -\int_{-\infty}^{\infty} d\varepsilon\, \varepsilon\, D_{qq'}(\varepsilon) = \int_{-\infty}^{\infty} d\varepsilon\, N_{qq'}(\varepsilon) \ , \tag{A7}$$

respectively. These relations may be derived by equating tight-binding expressions for the one-electron Hamiltonian matrix elements to $H^{\mathbf{k}}_{qq'} = \sum_j \alpha_{q\mathbf{k}j}\varepsilon_{\mathbf{k}j}\alpha^*_{q'\mathbf{k}j}$, and then averaging over the Brillouin zone. It is the latter average which removes hopping parameter contributions to the diagonal tight-binding matrix elements, since these are multiplied by phases $e^{i\mathbf{k}\cdot\mathbf{R}}$ which sum to zero. Similar cancellation can be important to Eq. (A7), which is best illustrated by the example given below.

The physical quantities $D(\varepsilon)$ and $\rho(\mathbf{r},\varepsilon_F)$ defined by Eqs. (A3) and (A4) are independent of orbital sign conventions. In presenting results for $D_{qq'}(\varepsilon)$, however, we shall multiply the right hand side of Eq. (A1) by the sign of $\phi_q(\mathbf{r})\phi_{q'}(\mathbf{r})$ near $\mathbf{r} = \frac{1}{2}(\mathbf{q}+\mathbf{q}')$, in order to preserve the convention of positive $D_{qq'}(\varepsilon)$ for bonding overlaps; negative, for antibonding. This leads to net positive area under $N_{qq'}(\varepsilon)$, $t_{qq'} > 0$ according to Eq. (A7), and thus requires the explicit use of $-t_{qq'}$ $(+t_{qq'})$ in tight-binding Hamiltonians to indicated bonding (antibonding) interactions. Also note that we have not explicitly acknowledged spin degeneracy, $\sigma = \pm 1$, which is most easily accommodated in the present paramagnetic treatment by letting q index spin orbitals, $q = \mathbf{q}nlm\sigma$, with the understanding that $D_{qq'}(\varepsilon)$, $N_{qq'}(\varepsilon)$, $t_{qq'} \propto \delta_{\sigma\sigma'}$.

Example

Both $A15$ Mo_3Si and $D8_m$ Mo_5Si_3 have **z**-direction near-neighbor Mo-Mo chains. A simple near-neighbor tight-binding treatment of their $d_{3z^2-r^2}$ states would be

$$H^{k_z} = \begin{pmatrix} \varepsilon_d & -t_{dd}(1+e^{ik_z a}) \\ -t_{dd}(1+e^{-ik_z a}) & \varepsilon_d \end{pmatrix} \ , \tag{A8}$$

where for convenience we have taken a basis of two Mo atoms, i.e., the chain goes –1–2–1′– where $\mathbf{R}_{1'} - \mathbf{R}_1 = a\hat{\mathbf{z}}$ is the shortest Bravais lattice vector. The two terms comprising $H^{k_z}_{21}$ correspond to the 2–1 and 2–1′ couplings, respectively. However, a Brillouin zone average of $H^{k_z}_{21}$ yields just $-t_{dd}$, the 2–1 interaction, just as the average of $H^{k_z}_{21'} \equiv H^{k_z}_{21}e^{ik_z a}$ yields the 2–1′ interaction, of course also $-t_{dd}$. Thus, it is important to note that Eq. (A1) may be used for couplings which cross the primitive cell boundary by multiplying the product $\alpha^*_{q'k}\alpha_{qk}$ by an appropriate phase $e^{i\mathbf{k}\cdot\mathbf{R}}$.

The off-diagonal number of states function corresponding to near-neighbor Mo-Mo overlaps in the chain described by Eq. (A8) is

$$N_{12}(\varepsilon) = \frac{1}{\pi}\sqrt{1-\left(\frac{\varepsilon-\varepsilon_d}{2t_{dd}}\right)^2}\ \theta\left(2t_{dd} - |\varepsilon-\varepsilon_d|\right) \ . \tag{A9}$$

In contrast, were there just two isolated atoms (or no 2–1′-like interactions between different primitive cells), the off-diagonal element of Eq. (A8) would be just $-t_{dd}$, and

$$N_{12}(\varepsilon) = \frac{1}{2}\,\theta\left(t_{dd} - |\varepsilon-\varepsilon_d|\right) \ . \tag{A10}$$

In both cases the area of $N_{12}(\varepsilon)$ is t_{dd}, which is the magnitude of the interaction between sites 1 and 2. However, for half-filled states, $\varepsilon_F = \varepsilon_d$, the respective values of $N_{12}(\varepsilon_F)$ are $1/\pi$ and $1/2$ indicating, according to Eq. (A4), less charge density in between two atoms in the chain than in between the two isolated atoms. This result is intuitively clear—the more bonds an atom tries to form, the less bond charge is available to any given one. The important point here, however, is the way Eqs. (A4) and (A7) formalize this behavior, namely that additional couplings to q or q' tend to spread out the state density associated with these orbitals, thereby generally reducing $N_{qq'}(\varepsilon)$ at any given ε since the area under this curve is conserved. Similarly, if the two states were not degenerate, the bond-antibond splitting for the isolated atom pair would grow from $2t_{dd}$ to $\sqrt{(\varepsilon_2-\varepsilon_1)^2+4t^2_{dd}}$, also reducing $N_{qq'}(\varepsilon)$.

The total midbond charge density for the chain described by Eq. (A8) would go as $\rho(\mathbf{r}_b,\varepsilon) = 2[N_{11}(\varepsilon) + N_{22}(\varepsilon)+2N_{12}(\varepsilon)]\,\phi_1(\mathbf{r}_b)^2$, where the factor of 2 is for spin degeneracy and $\phi_1(\mathbf{r}_b) = \phi_2(\mathbf{r}_b)$. The diagonal functions $N_{11}(\varepsilon) = N_{22}(\varepsilon)$ corresponding to Eqs. (A9) and (A10) are $(1/\pi)\cos^{-1}[(\varepsilon_d-\varepsilon)/2t_{dd}]$ and $1/2$, respectively, in the range of the respective step functions. This illustrates the requirement $d\rho(\mathbf{r},\varepsilon)/d\varepsilon \geq 0$, and suggests that off-diagonal terms contribute up to half of the midbond charge density.

[1] T. W. Barbee, Jr., S. Mrowka, and M. C. Hettrick, Appl. Opt. **24**, 883 (1985).
[2] N. M. Ceglio, J. X-Ray. Sci. Technol. **1**, 7 (1989).
[3] A. K. Petford-Long, M. B. Stearns, C.-H. Chang, S. R. Nutt, D. G. Stearns, N. M. Ceglio, and A. M. Hawrylak, J. Appl. Phys. **61**, 1422 (1987).
[4] K. Holloway, H. B. Do, and R. Sinclair, J. Appl. Phys. **65**, 474 (1989).
[5] D. G. Stearns, M. B. Stearns, Y. Cheng, J. H. Stith, and N. M. Ceglio, J. Appl. Phys. **67**, 2415 (1990).
[6] J. M. Slaughter, A. Shapiro, P. A. Kearney, and C. M. Falco, Phys. Rev. B **44**, 3854 (1991).
[7] S. P. Murarka, *Silicides for VLSI Applications* (Academic, New York, 1983).
[8] M. A. Nicolet and S. S. Lau, in *VLSI Electronics: Microstructure Science* (Academic, New York, 1983), Vol. 6, p. 329.
[9] K. Shibata, S. Shima, and M. Kashiwagi, J. Electrochem. Soc. **129**, 1527 (1982).
[10] A. Perio and J. Torres, J. Appl. Phys. **59**, 2760 (1986); A. Perio, J. Torres, G. Bomchil, F. Arnaud d'Avitaya, and R. Pantel, Appl. Phys. Lett. **45**, 857 (1984).
[11] J. Y. Cheng, H. C. Cheng, and L. J. Chen, J. Appl. Phys. **61**, 2218 (1987).
[12] C. M. Doland and R. J. Nemanich, J. Mater. Res. **5**, 2854 (1990).
[13] T. C. Chou and T. G. Nieh, Thin Solid Films **214**, 48 (1992).
[14] P. J. Meschter and D. S. Schwartz, J. Met. **41** (11), 52 (1989).
[15] *Intermetallic Matrix Composites II*, edited by D. B. Miracle, D. L. Anton, and J. A. Graves, MRS Symposia Proceedings No. 273 (Materials Research Society, Pittsburgh, 1992).
[16] J. J. Petrovic, MRS Bull. **18**, 35 (1993); A. K. Vasudévan and J. J. Petrovic, Mater. Sci. Eng. A **155**, 1 (1992).
[17] T. C. Lu, A. G. Evans, R. J. Hecht, and R. Mehrabian, Acta Metall. Mater. **39**, 1853 (1991).
[18] T. Hong, J. R. Smith, and D. J. Srolovitz, Interf. Sci. **1**, 223 (1993).
[19] See, e.g., 15 papers on $MoSi_2$-based materials in Mater. Sci. Eng. A **155** (1992).
[20] W. L. Morgan and D. B. Boercker, Appl. Phys. Lett. **59**,1176 (1991).
[21] See, e.g., a recent tight-binding representation of the total energy for Ni, Co, and Fe disilicides: G. Malegori and L. Miglio, Phys. Rev. B **48**, 9223 (1993).
[22] *Binary Alloy Phase Diagrams*, edited by T. B. Massalski, 2nd ed. (American Society for Metals, Materials Park, 1990), Vol. 3, p. 2664.
[23] B. K. Bhattacharyya, D. M. Bylander, and L. Kleinman, Phys. Rev. B **31**, 2049 (1985); **31**, 5462 (1985).
[24] L. F. Mattheiss, Phys. Rev. B **43**, 1863 (1991).
[25] O. Bisi and C. Calandra, J. Phys. C **14**, 5479 (1981).
[26] Y. J. Chabal, D. R. Hamann, J. E. Rowe, and M. Schlüter, Phys. Rev. B **25**, 7598 (1982).
[27] J. Tersoff and D. R. Hamann, Phys. Rev. B **28**, 1168 (1983).
[28] W. R. L. Lambrecht, N. E. Christensen, and P. Blöchl, Phys. Rev. B **36**, 2493 (1987).
[29] K. A. Mäder, H. von Känel, and A. Baldereschi, Phys. Rev. B **48**, 4364 (1993).
[30] P. S. Ho, G. W. Rubloff, J. E. Lewis, V. L. Moruzzi, and A. R. Williams, Phys. Rev. B **22**, 4784 (1980).
[31] J. H. Weaver, V. L. Moruzzi, and F. A. Schmidt, Phys. Rev. B **23**, 2916 (1981).
[32] J. H. Weaver, A. Franciosi, and V. L. Moruzzi, Phys. Rev. B **29**, 3293 (1984).
[33] B. K. Bhattacharyya, D. M. Bylander, and L. Kleinman, Phys. Rev. B **32**, 7973 (1985).
[34] M. J. Zhu, D. M. Bylander, and L. Kleinman, Phys. Rev. B **36**, 3182 (1987).
[35] Shaoping Tang, Kaiming Zhang, and Xide Xi, J. Phys. C **21**, L777 (1988); Tang Shaoping and Zhang Kaiming, *ibid.* **21**, 1469 (1988).
[36] M. Alouani, R. C. Albers, and M. Methfessel, Phys. Rev. B **43**, 6500 (1991).
[37] A. E. Carlsson and P. J. Meschter, J. Mater. Res. **6**, 1512 (1991).
[38] L. F. Mattheiss, Phys. Rev. B **45**, 3252 (1992).
[39] L. F. Mattheiss, Phys. Rev. B **43**, 12 549 (1991).
[40] T. Jarlborg and G. Arbman, J. Phys. F **6**, 189 (1976); **9**, 1635 (1977).
[41] B. M. Klein, L. L. Boyer, D. A. Papaconstantopoulos, and L. F. Mattheiss, Phys. Rev. B **18**, 6411 (1978).
[42] W. E. Pickett, K. M. Ho, and M. L. Cohen, Phys. Rev. B **19**, 1734 (1979); K. M. Ho, W. E. Pickett, and M. L. Cohen, *ibid.* **19**, 1751 (1979).
[43] O. Bisi and L. W. Chiao, Phys. Rev. B **25**, 4943 (1982).
[44] M. Methfessel, Phys. Rev. B **38**, 1537 (1988).
[45] M. Methfessel, C. O. Rodriguez, and O. K. Andersen, Phys. Rev. B **40**, 2009 (1989).
[46] R. S. Mulliken, J. Chem. Phys. **23**, 1833 (1955); T. Hughbanks and R. Hoffmann, J. Am. Chem. Soc. **105**, 3528 (1983); R. Hoffmann, Rev. Mod. Phys. **60**, 601 (1988).
[47] See, e.g., pp. A1–A5 in Ref. 22.
[48] *International Tables for Crystallography*, Vol. A, *Space-Group Symmetry*, edited by Theo Hahn, 2nd ed. (Kluwer Academic, Dordrecht, 1989).
[49] P. Villars and L. D. Calvert, *Pearson's Handbook of Crystallographic Data for Intermetallic Phases* (American Society for Metals, Metals Park, 1985).
[50] The $D8_m$ and $A15$ structures are related by a Hyde rotation, see, P. E. A. Turchi and A. Finel, Phys. Rev. B **46**, 702 (1992).
[51] O. K. Andersen, Phys. Rev. B **12**, 3060 (1975).
[52] H. L. Skriver, *The LMTO Method* (Springer, Berlin, 1984).
[53] L. Hedin and B. I. Lundqvist, J. Phys. C **4**, 2064 (1971). A generalization allowing spin-polarized calculations is given in V. L. Moruzzi, J. F. Janak, and A. R. Williams, *Calculated Electronic Properties of Metals* (Pergamon, New York, 1978).
[54] J. Birch, J. Geophys. Res. **83**, 1257 (1978).
[55] See, e.g., P. Bagno, O. Jepsen, and O. Gunnarsson, Phys. Rev. B **40**, 1997 (1989), and references therein.
[56] V. Fiorentini, M. Methfessel, and M. Scheffler, Phys. Rev. B **47**, 13 353 (1993). See Appendix.
[57] O. K. Andersen and O. Jepsen, Phys. Rev. Lett. **53**, 2571 (1984).
[58] C. Kittel, *Introduction to Solid State Physics*, 6th ed. (Wiley, New York, 1986).
[59] K. W. Katahara, M. H. Manghnani, and E. S. Fisher, J. Phys. F **9**, 773 (1979).
[60] M. Nakamura, S. Matsumoto, and T. Hirano, J. Mater. Sci. **25**, 3309 (1990).
[61] Based on measured Debye temperatures of 454, 759, and 576 K [Ref. 60 and K. A. Gschneidner, Jr., Solid State Phys. **16**, 275 (1964), Table XVI], Debye model estimates of 298-K lattice vibrational corrections to the total energy

are $\Delta E_{\rm lat}^{298} = 0.09$, 0.10, and 0.09 eV/atom, for Mo, $MoSi_2$, and Si, respectively. Similarly, thermal corrections $\Delta E_{\rm lat}^{298} - \Delta E_{\rm lat}^{0}$ suggest $\Delta H_f^{298} - \Delta H_f^0 \sim 0.01$ eV/atom for $MoSi_2$.

[62] We estimate zero-point expansion of V_0 to be $\Delta V/V_0 \sim \gamma \Delta E_{\rm lat}^0/(V_0 B_0) \sim 0.35\%$, 0.84%, 0.90%, for Mo, $MoSi_2$, and Si, respectively, based on Slater model [J. C. Slater, *Introduction to Chemical Physics* (McGraw-Hill, New York, 1939), Chaps. XIII and XIV] values of γ (~ 2 in each case) obtained from the volume dependence of our calculated total energies. Thermal expansion ($0 \rightarrow 298$ K) accounts for additional 0.3%, 0.39%, and 0.07% increases in volume for Mo, $MoSi_2$, and Si, respectively [*American Institute of Physics Handbook*, edited by D. E. Gray, 3rd ed. (McGraw-Hill, New York, 1972); O. Thomas *et al.*, Solid State Commun. **55**, 629 (1985)].

[63] H. J. Goldschmidt, *Interstitial Alloys* (Plenum, New York, 1967).

[64] T. G. Chart, Met. Sci. **8**, 344 (1974).

[65] R. Pretorius, J. M. Harris, and M.-A. Nicolet, Solid-State Electron. **21**, 667 (1978).

[66] G. V. Samsonov and I. M. Vinitskii, *Handbook of Refractory Compounds* (Plenum, New York, 1980).

[67] A. García, C. Elsässer, J. Zhu, S. G. Louie, and M. L. Cohen, Phys. Rev. B **46**, 9829 (1992).

[68] J. P. Perdew, J. A. Chevary, S. H. Vosko, K. A. Jackson, M. R. Pederson, D. J. Singh, and C. Fiolhais, Phys. Rev. B **46**, 6671 (1992).

[69] W. A. Harrison, *Electronic Structure and the Properties of Solids* (Dover, New York, 1989).

[70] S. J. Duclos, Y. K. Vohra, and A. L. Ruoff, Phys. Rev. Lett. **58**, 775 (1987); Phys. Rev. B **41**, 12 021 (1990).

[71] A. K. McMahan and J. A. Moriarty, Phys. Rev. B **27**, 3235 (1983).

[72] A. K. McMahan, J. F. Annett, and R. M. Martin, Phys. Rev. B **42**, 6268 (1990).

[73] Using fifth-power scaling of $V_{dd\sigma}$ to the second neighbor distance yields $|V_{dd\sigma}/V_{pd\sigma}| = 0.7$ at that distance for the $A15$ phase, while our $C11_b$ results give $|V_{pd\sigma}/V_{pp\sigma}| = 0.7$ at the first neighbor distance in that phase.